NASA Technical Paper 3194

1992

Wind-Tunnel Static and Free-Flight Investigation of High-Angle-of-Attack Stability and Control Characteristics of a Model of the EA-6B Airplane

Frank L. Jordan, Jr.,
and David E. Hahne
Langley Research Center
Hampton, Virginia

National Aeronautics and Space Administration
Office of Management
Scientific and Technical Information Program

Summary

An investigation was conducted in the Langley 30- by 60-Foot Tunnel and the Langley 12-Foot Low-Speed Tunnel to identify factors contributing to a directional divergence at high angles of attack for the EA-6B airplane and to evaluate airframe modifications that would eliminate or delay the instability to angles of attack farther removed from the flight envelope. The study consisted of static wind-tunnel tests, smoke and tuft flow-visualization tests, and free-flight tests of a 1/8.5-scale model of the airplane. The results of the investigation indicated that the directional divergence of the airplane was brought about by a loss of directional stability and effective dihedral at high angles of attack. The loss of directional stability was caused by an adverse sidewash at the aft fuselage and vertical tail location; the sidewash was produced by a vortex system originating near the fuselage-wing juncture. The loss of effective dihedral was attributed to a combination of stalling of the leading wing panel during sideslip at high angles of attack and the effect of the adverse sidewash on the vertical tail. Modifications that significantly alleviated the stability problem were an inboard wing-leading-edge droop, a glove strake, and a vertical-tail extension. The results of the free-flight study showed that the modified configuration exhibited good dynamic stability characteristics and could be flown at angles of attack significantly higher than those of the unmodified configuration.

Introduction

The NASA Langley Research Center, in response to a request from the U.S. Navy, is currently conducting a broad cooperative research program with the Grumman Aircraft Systems Division of the Grumman Corporation to improve the maneuverability of the EA-6B airplane (refs. 1 to 5). A primary factor limiting the maneuverability of the airplane has been continual growth in takeoff, combat, and landing weights in recent years coupled with no increase in wing lifting capability. This constraint has resulted in operational angles of attack very near stall, and the reduced stall margin has seriously limited the maneuvering capability of the airplane.

The maneuvering capability is further degraded by a loss in directional stability at angles of attack near stall. This directional instability, combined with a loss of lateral stability and control near stall, results in a roll-off followed by a directional divergence (sometimes termed "nose slice"). Further penetration of the stall will lead to post-stall gyrations that may develop into a spin. Whereas previous investigations have concentrated on improving the high-angle-of-attack aerodynamic characteristics of the takeoff and powered approach configuration (unpublished in-house Grumman report), the present NASA-Grumman program includes a series of investigations focused primarily on improving the characteristics of the cruise configuration. The program includes investigations in low-speed wind tunnels to improve the configuration stability and control and in high-speed wind tunnels to verify the computational design of wing leading- and trailing-edge sections to increase low-speed lift capability while maintaining high-speed cruise performance.

This report presents the results of the low-speed wind-tunnel investigation to improve the high-angle-of-attack stability and control characteristics of the airplane. The investigation, which was conducted in the Langley 30- by 60-Foot Tunnel and the Langley 12-Foot Low-Speed Tunnel, consisted of static force, flow-visualization, and dynamically scaled free-flight tests of a 1/8.5-scale model. This paper concentrates on the results of the static force tests with emphasis on the development of the configuration modifications for improved stability and control at high angles of attack. The objectives of the tests were (1) to identify the various factors contributing to the directional divergence, (2) to define geometric modifications that could be easily implemented on the fleet aircraft to increase lateral stability and eliminate or delay the directional instability to higher angles of attack, and (3) to define and evaluate concepts that maintain adequate levels of lateral control beyond stall.

Symbols and Abbreviations

The longitudinal aerodynamic forces and moments are referred to the stability-axis system, and all lateral-directional data are referred to the body-axis system shown in figure 1. All static force and moment data are referenced to a center-of-gravity position of $0.253\bar{c}$.

b	wing span, ft
C_D	drag coefficient, $\frac{\text{Drag}}{q_\infty S}$
C_L	lift coefficient, $\frac{\text{Lift}}{q_\infty S}$
C_l	rolling-moment coefficient, $\frac{\text{Rolling moment}}{q_\infty S b}$
C_m	pitching-moment coefficient, $\frac{\text{Pitching moment}}{q_\infty S \bar{c}}$
C_n	yawing-moment coefficient, $\frac{\text{Yawing moment}}{q_\infty S b}$
C_Y	side-force coefficient, $\frac{\text{Side force}}{q_\infty S}$

c	local wing chord, ft
$\bar{c}$	mean aerodynamic chord, ft
g	acceleration due to gravity, 32.174 ft/sec^2
I_X, I_Y, I_Z	moments of inertia about X-, Y-, and Z-axis, respectively, slug/ft^2
K_p	roll-rate feedback gain to flaperon, sec
K_q	pitch-rate feedback gain to horizontal tail, sec
K_r	yaw-rate feedback gain to rudder, sec
$K_{R,\beta}$	sideslip-angle feedback gain to flaperon
$K_{Y,\beta}$	sideslip-angle feedback gain to rudder
p	roll rate, deg/sec
q	pitch rate, deg/sec
q_∞	free-stream dynamic pressure, lb/ft^2
r	yaw rate, deg/sec
S	wing reference area, ft^2
s	frequency-domain independent variable
V	free-stream velocity, ft/sec
X, Y, Z	body reference axes
x	chordwise distance from wing leading edge, positive aft, ft
z	vertical distance from wing leading edge, positive up, ft
α	angle of attack, deg
β	angle of sideslip, deg
ΔC_l	incremental rolling-moment coefficient
ΔC_n	incremental yawing-moment coefficient
ΔC_Y	incremental side-force coefficient
δ_f	flaperon deflection angle, positive with trailing edge up, deg
δ_h	horizontal-tail deflection angle, positive with trailing edge down, deg
δ_r	rudder deflection angle, positive with trailing edge left, deg
$\delta_{S/B}$	speed-brake deflection angle, upper panel positive with trailing edge up, lower panel positive with trailing edge down, deg

Subscripts:

u	upper surface
l	lower surface

Abbreviations:

c.g.	center of gravity
W.S.	model wing station, in.
SAS	stability augmentation system

Model component designations:

L	lower speed-brake panel
LE	wing leading edge
TE	wing trailing edge
U	upper speed-brake panel

Stability derivatives:

$$C_{l_\beta} = \frac{\partial C_l}{\partial \beta} \qquad C_{n_\beta} = \frac{\partial C_n}{\partial \beta} \qquad C_{Y_\beta} = \frac{\partial C_Y}{\partial \beta}$$

$$C_{n_{\delta_r}} = \frac{\partial C_n}{\partial \delta_r} \qquad C_{l_{\delta_f}} = \frac{\partial C_l}{\partial \delta_f}$$

$$C_{n_{\beta,\mathrm{dyn}}} = C_{n_\beta} \cos\alpha - \frac{I_Z}{I_X} C_{l_\beta} \sin\alpha$$

Description of Airplane Configuration

The airplane configuration is a four-place subsonic twin-jet airplane with electronic countermeasures and is designed for land- and carrier-based operations. The configuration tested was the proposed advanced-capability version, which has an enlarged fin pod, an additional outboard store station on each wing, and an additional antenna group located under the fuselage. A three-view sketch of the model showing the general layout of the configuration is presented in figure 2. The longitudinal control system of the airplane consists of an all-movable horizontal tail (stabilizer), the roll control system consists of flaperons (commonly called spoilers) on the upper surface of the wing, deflected on the down-going wing only (fig. 3), and the directional control system consists of a conventional rudder. The airplane is also equipped with speed brakes, which consist of upper and lower wing-tip panels deflected as shown in figure 4. The maximum control-surface deflections are as follows:

Rudder deflection, deg:	
Clean	±4 (augmented ±35 for spin recovery)
Flaps down	±23
Stabilizer deflection (leading edge), deg:	
Clean	1.5 up, 10 down
Flaps down	1.5 up, 24 down
Flaperon deflection, deg	51 up
Maximum leading-edge slat deflection, deg	27 down
Maximum flap deflection, deg	30 down

Model and Tests

Model Description

The wind-tunnel data presented herein were obtained with a 1/8.5-scale model representing the proposed advanced-capability configuration. The model was constructed primarily of molded fiberglass and was fabricated such that individual model airframe components could be tested separately and in several combinations to determine their contributions to the overall stability characteristics of the airplane and to determine mutual interference effects. Stores and pylons were also removable in order to study their contributions to the aerodynamic characteristics of the airplane. The model was dynamically scaled for the free-flight tests. The mass and geometric characteristics of the model are listed in table I, and a photograph of the model is presented in figure 5. For the static force data presented herein, the horizontal tail was set at a nominal trim position of $\delta_h = -5°$, and the centerline store was removed because of interference with the model support.

A number of geometric modifications to the basic airplane configuration were developed and evaluated as candidate improvements in the lateral-directional stability during the course of the test program. Three of the modifications, which produced beneficial effects, are discussed herein. These modifications consisted of a wing-fuselage strake extending from the leading edge of the wing root glove, an inboard wing-leading-edge droop extending from model W.S. 9.41 in. to W.S. 16.89 in., and a vertical-tail (fin) extension. Photographs showing these modifications installed on the model are presented in figure 6, and detailed sketches of the modifications are presented in figure 7.

In addition to these modifications to improve the lateral-directional stability, computationally designed wing-leading- and trailing-edge sections that were developed concurrently in high-speed tests to increase maximum wing lift and improve high-speed performance (ref. 5) were also incorporated into the present investigation. These leading- and trailing-edge modifications extended over the spans of the slat and flap. The modified sections are shown in the sketch in figure 8. The airfoil coordinates at the inboard and outboard design stations for the basic wing and for the wing with leading- and trailing-edge modifications are given in tables II and III, respectively. Further details of the leading- and trailing-edge modifications are given in reference 5.

The airfoil coordinates at the inboard design station for the wing with the inboard leading-edge droop are given in table IV. The inboard droop extended the wing chord 2 percent and modified the lower surface contour back to $0.15c$. The droop modification was tested on both the basic wing and on the wing with the leading- and trailing-edge modifications. The coordinates in table IV are for the case with both modifications included.

Also, as the investigation progressed, it became clear that an improvement in roll control power would be required in order to realize the benefits from improved stability levels. Roll control augmentation was therefore explored in the test program through investigation of the use of the airplane's existing speed brakes as ailerons on the model. The model speed brakes were modified to be used as typical ailerons, as shown in figure 9, by deflecting either one panel individually or by deflecting upper and lower panels together.

Finally, in order to evaluate the effect of the modifications on the takeoff and powered approach configuration, the model incorporated slats and trailing-edge flaps that could be deflected 27° and 30°, respectively.

Force Tests

Tests were conducted in the Langley 12-Foot Low-Speed Tunnel and the Langley 30- by 60-Foot Tunnel at dynamic pressures of 4 lb/ft^2 and 10 lb/ft^2, respectively, which correspond to Reynolds numbers of 0.47×10^6 and 0.75×10^6 based on the wing mean chord. In these tests, body-axis forces and moments were measured with a conventional strain gage balance and were resolved into the appropriate aerodynamic coefficients. The static force tests included a component buildup and were made over an angle-of-attack range of $-2°$ to 40° and an angle-of-sideslip range of $-5°$ to 5°.

Flow-visualization tests were also conducted with both tuft and smoke techniques. Surface tufts yielded information about the surface airflow over the model,

and the smoke technique and a tuft wand gave information about the off-surface flow field. The primary objective of the flow-visualization tests was to develop an understanding of flow mechanisms contributing to the directional stability problem at high angles of attack.

The development of each of the geometric modifications for improved lateral-directional stability characteristics involved many test runs in which the size, shape, and location of the modification were changed by small amounts until the maximum improvement was obtained. In general, the modifications were first oversized in the initial test runs in order to obtain a definite effect. Then they were optimally located and tailored to the smallest possible size that would result in a substantial improvement in lateral-directional stability without degrading the longitudinal characteristics. In the interest of brevity, only static force and moment test data showing the effects from the final, optimized modifications are presented in this paper. Because of the relatively low Reynolds number of the present tests, no performance data are presented, and unless otherwise noted the data are taken from the tests in the Langley 12-Foot Low-Speed Tunnel.

Free-Flight Tests

The model was dynamically scaled and flown in the open-throat test section of the Langley 30- by 60-Foot Tunnel in order to assess the effects of the airframe modifications on general flying characteristics and on stability and control. A sketch showing the test setup for the free-flight tests is shown in figure 10, and a photograph of the model in free flight is presented in figure 11. The model was remotely controlled by three pilots: a roll and yaw pilot, a pitch pilot, and a thrust operator. Pneumatic and electric power and control signals were supplied to the model through a flexible umbilical cord that was made up of wires and light plastic tubes. The umbilical cord also incorporated a 1/8-in.-diameter steel safety cable that passed through a pulley above the test section. The safety cable was used to catch the model when an uncontrollable motion or a mechanical failure occurred. The entire umbilical cord was kept slack during the flights by a safety cable operator using a high-speed winch.

The model was instrumented with a three-axis rate gyroscope to measure angular rates and a miniaturized boom-mounted vane sensor to measure angles of attack and sideslip. These data, along with pilot control inputs and control-surface deflections, were recorded in time-history form on strip-chart recorders. Also, qualitative assessments of the model flight characteristics were taken in the form of motion pictures and pilot comments. A more detailed discussion of the free-flight test technique can be found in reference 6.

The flight control laws, which included stability augmentation about all three axes, were programmed into a digital computer that processed sensor data and pilot control inputs to generate command signals to drive the electropneumatic control-surface actuators in the model. Diagrams of the control laws used in this investigation are presented in figure 12, and the stability augmentation system (SAS) gains are given in the following table:

Configuration	K_p, sec	$K_{R,\beta}$	K_r, sec	$K_{Y,\beta}$
Normal operation				
Cruise	0.274	0	0.283	0
Takeoff and landing	0.274	0	0.283	0
High-angle-of-attack operation				
Cruise	1.096	3.0	1.50	−3.0
Takeoff and landing	0.822	0	1.50	0

The normal rate feedback gains are scaled representations of the gain levels for the actual aircraft. Because of the higher rates associated with the subscale model, the gains were also scaled to account for this effect. A further discussion of scaling relationships can be found in reference 7.

The free-flight tests were made to determine the dynamic stability and control characteristics of the basic model configuration and of the modified configurations at high angles of attack. These tests included steady $1g$ flights at angles of attack between 10° and 27° and $1g$ stalls. All free-flight tests were made with a model center-of-gravity location of $0.233\bar{c}$. This center-of-gravity location corresponds to a typical weight condition for the landing transition with a full store complement.

The highlights of the flight test results are presented in this paper and consist mainly of qualitative pilot observations and opinions of the behavior of the model. Motion-picture records were made of all flights, and quantitative data obtained from the vane sensor records in the form of model angle of attack and angle of sideslip are discussed.

Results and Discussion of Force and Moment Tests

Longitudinal Stability Characteristics

Basic configuration. The static longitudinal characteristics obtained during the force tests on the unmodified cruise configuration are presented in figure 13. The variation of lift coefficient with angle of attack for the cruise configuration shows that the lift-curve slope begins to decrease at an angle of attack of about 10°. The variation of pitching moment with angle of attack indicates a region of neutral longitudinal stability from about 8° to 10°, which is followed by a stable break at higher angles of attack.

Photographs from the tuft studies of the cruise configuration showing the progression of wing stall are presented in figure 14. The flow separation beginning at the wing trailing edge and wing tips and progressing over the outer wing panel causes the decrease in the lift-curve slope and the reduction in the level of longitudinal stability noted in figure 13. The significance of the longitudinal aerodynamic characteristics is that the progression of major wing stall is reflected in changes in the lateral-directional aerodynamic characteristics, which is discussed subsequently.

The variation of lift coefficient with angle of attack for the unmodified takeoff powered approach configuration (leading-edge-slat and trailing-edge-flap deflections of 27° and 30°, respectively) shows a slight decrease in the lift-curve slope at an angle of attack of 4° and a large decrease starting at 12°, with maximum lift occurring at about 20° (fig. 15). A region of slightly unstable pitching moment is present for angles of attack of 12° to 20° and is followed by a stable break at higher angles of attack.

Effects of modifications. The effects of the combined modifications on the longitudinal characteristics of the basic configuration are shown in figure 16. The data in figure 16 include the effects of the inboard wing-leading-edge droop, the leading-edge glove strake, the vertical-tail (fin) extension, and the modified wing-leading- and trailing-edge sections.

Figure 16(a) shows that for the cruise configuration the modifications increase the slope of the lift curve and improve the poststall lift significantly. The modified wing sections rely heavily on trailing-edge camber and increased leading-edge radius or droop to improve maximum wing lift. Since both of these section design characteristics are very dependent on Reynolds number (refs. 3 and 5), the performance of the wing airfoil modifications would be expected to improve with the higher Reynolds numbers in flight.

As shown in figure 16(b) the modifications have a negligible effect on the lift curve of the takeoff powered approach configuration but improve longitudinal stability near the stall by eliminating the neutral-to-unstable trend noted for the unmodified configuration.

Lateral-Directional Stability and Control

Basic configuration. The static lateral-directional stability derivatives obtained over sideslip angles of −5° to 5° for the unmodified configuration are summarized in figure 17. The values of the stability derivatives are presented as the variations with angle of attack of the side-force derivative C_{Y_β}, the directional-stability derivative C_{n_β}, and the effective-dihedral derivative C_{l_β}. The data for the cruise configuration (fig. 17(a)) indicate a marked decrease in C_{n_β} as angle of attack is increased, with the configuration becoming directionally unstable (negative values of C_{n_β}) at angles of attack above 15°. The data also indicate that as the angle of attack exceeds about 14°, a substantial reduction in effective dihedral occurs. The loss of directional stability at $\alpha = 15°$ is considered to be particularly significant because of the subsequent loss of effective dihedral (positive values of C_{l_β}) at an angle of attack of about 17°. A vertical cross-hatched region indicating the maximum trim capability of the horizontal tail ($\delta_h = -10°$), based on data from the Langley 30- by 60-Foot Tunnel presented in figure 18, is also shown in figure 17(a). As shown, a trim-angle-of-attack range of 3° exists for which the airplane is directionally unstable.

The stability derivatives for the takeoff powered approach configuration are presented in figure 17(b). Although this configuration also exhibits a marked directional instability at high angles of attack, C_{n_β} remains positive to almost $\alpha = 19°$. Also, these data indicate that values of C_{l_β} remain negative (positive dihedral effect) throughout the angle-of-attack range.

Some selected results of tests to evaluate the contributions of various airframe components to the lateral-directional stability derivatives are summarized in figure 19. Data obtained for the isolated fuselage and for the wing-fuselage combination are presented as well as data showing the effects resulting from the addition of the vertical-tail surface to the fuselage and the wing-fuselage combination. Several points can be noted from comparisons of various data. For example, the data show that the isolated fuselage becomes less directionally unstable (relative to body-axis moments) as angle of attack is increased. The wing-fuselage combination, however,

shows increasingly unstable variations of C_{n_β} with increasing angle of attack. The data also show that the contribution of the vertical tail to directional stability is greatly diminished as the angle of attack is increased above 17°, and the tail actually becomes destabilizing at angles of attack above 22°. An examination of the C_{l_β} data indicates that as the angle of attack exceeds about 14°, a large reduction in effective dihedral occurs for the wing-fuselage combination, and C_{l_β} becomes unstable at about 22°. As with the directional data, the stabilizing contribution of the vertical tail to C_{l_β} diminishes as the angle of attack is increased above stall and the tail becomes destabilizing above about 22°.

Flow-visualization studies. The large unstable variation of directional stability for swept-wing–fuselage combinations at high angles of attack is known to be due primarily to wing or wing-induced sidewash over the fuselage afterbody. (See refs. 8 and 9.)

In order to diagnose the flow mechanisms contributing to the directional instability near stall, flow-visualization studies were conducted by injecting smoke into the airstream ahead of the model, by exploring with a long streamer on a wand, and by installing a tufted vertical rod in place of the vertical tail. The first two techniques were used to identify general flow-field characteristics (regions of separated flow, vortex flow, upwash, downwash, etc.) in the vicinity of the model. The third technique was used to determine flow angularity at the location of the vertical tail.

Results from these studies show that a pair of vortices are generated at the fuselage-wing junctures. These vortices trail behind the wing, close to the fuselage and below the tail at low angles of attack (fig. 20(a)). As the angle of attack is increased, wing downwash maintains the vortex system at the same relative location, that is, low with respect to the vertical tail. At stall angles of attack, flow separation on the wing and consequent downwash breakdown cause the vortices to rise to the level of the vertical tail (fig. 20(b)). In sideslip, the vortex generated on the windward side of the airplane drifts leeward such that as the angle of attack is increased through stall, the vertical tail becomes immersed in the windward vortex flow field (fig. 20(c)). Because of the rotational sense of the vortex system, the bottom portion of the vertical tail first becomes immersed in a region of proverse (stabilizing) sidewash—the top portion of the windward vortex. As the angle of attack is increased and the vortex system rises farther, the vertical tail becomes immersed in the lower portion of the windward vortex, where a condition of adverse (destabilizing) sidewash exists. Clearly, the abrupt changes in sidewash that occur as the windward vortex traverses the span of the vertical tail have a direct impact on directional stability. In fact, it is this phenomenon that causes the directional instability the airplane configuration experiences near stall. This fact is evident in figure 19, where the contributions of the vertical tail to directional stability both in the presence of the fuselage alone and in the presence of the fuselage-wing combination are compared. At low angles of attack the stabilizing effect of the vertical tail is amplified by the proverse sidewash in the top portion of the windward vortex. At stall angles of attack ($16° < \alpha < 24°$), the adverse sidewash in the lower portion of the vortex has the opposite effect—that is, the vertical tail abruptly becomes highly destabilizing. It is also clear that the condition of adverse sidewash on the vertical tail is a factor contributing to the loss of effective dihedral at $\alpha = 17°$. This is shown in figure 19, where at low angles of attack the presence of the tail has a stabilizing effect due to the proverse sidewash of the top portion of the windward vortex, but at high angles of attack the adverse sidewash causes the stable contribution of the vertical tail to diminish and, at $\alpha = 22°$, the tail becomes destabilizing.

Tuft studies were also conducted as an aid in interpreting the static force results. Photographs of the tuft patterns on the left wing at an angle of attack of 20° for sideslip angles of 10° and −10° are presented in figure 21. Whereas the flow remains attached on part of the inboard trailing wing panel (photograph at $\beta = 10°$), the tufts indicate complete stall and a region of reversed flow behind the leading wing panel ($\beta = -10°$). The adverse-flow region on the fuselage behind the wing is a major factor contributing to the reduction in directional stability of the wing-fuselage combination at high angles of attack. These results are in agreement with the off-surface flow-visualization tests using the smoke and wand techniques, as shown in figure 20. The results of the tuft studies indicate that stall of the leading wing panel is also a major factor contributing to the loss of effective dihedral at $\alpha = 17°$. This result is a characteristic of swept wings at high angles of attack.

Control effectiveness. The results of tests to determine the effectiveness of the rudder and flaperons for the basic cruise configuration are presented in figures 22 and 23. The flaperons, which are spoiler-like surfaces on the upper surface of the wing, are the basic lateral control system for the airplane. The data are presented in terms of incremental values of C_l, C_n, and C_Y produced by a right-roll or

right-yaw control deflection. Figure 22 shows the incremental forces and moments produced by rudder deflections from $-5°$ to $-35°$. The data show that the rudder remains very effective at an angle of attack of 15°, where directional stability becomes zero. This result indicates that the dynamic pressure at the tail is maintained and provides further evidence that the degradation in vertical-tail contribution to directional stability is caused primarily by adverse sidewash. The values of ΔC_Y, ΔC_n, and ΔC_l produced by the maximum flaperon deflection ($\delta_f = 51°$, fig. 23) show that a rapid loss of available roll-control power occurs at angles of attack beyond stall.

Effect of modifications. As previously mentioned, a major portion of this investigation focused on identifying aerodynamic modifications that would eliminate or postpone to higher angles of attack the directional instability the airplane experiences near the stall angle. Since it was determined that adverse flow from the wing-fuselage combination is a major factor causing the directional instability, tests were first conducted to modify the basic wing aerodynamics. An approach was suggested by the fact that more stable static stability results are noted for the takeoff powered approach configuration than for the cruise configuration. That is, when leading-edge slats and flaps are extended, values of C_{n_β} are stable to higher angles of attack than when the slats and flaps are retracted and C_{l_β} remains stable throughout the angle-of-attack range. (See fig. 17(b).) Therefore, an attempt was made to simulate the effect of the leading-edge slats through incorporation of various leading-edge droop extensions on the wing. The most effective arrangement is the inboard wing-leading-edge droop that was described previously (fig. 7(b)). The results of tests showing the effects of this modification on C_{n_β} and C_{l_β} are presented in figure 24. The data indicate that leading-edge droop produces two beneficial effects. First, the angle of attack at which directional stability becomes zero is increased slightly and the levels of instability at higher angles of attack are reduced; and second, C_{l_β} does not become unstable throughout the test angle-of-attack range (up to $\alpha = 40°$). These effects are believed to be related to a delay in the stall progression on the inboard panel of the leading wing in sideslip. This delay increases the dihedral effect and increases the angle of attack at which the previously described trailing vortex system rises. These changes have important beneficial effects on dynamic lateral-directional stability, as is shown subsequently.

To further modify the inboard wing aerodynamics, several strakes were tested in the location near the wing-glove fuselage junction. The most effective arrangement is the small triangular strake described previously (fig. 7(a)). The effects of this modification on C_{n_β} and C_{l_β} are shown in figure 25. The angle of attack at which directional stability becomes zero is increased to nearly 17°, and small reductions in the levels of instability are present to $\alpha = 25°$. The strake also produces favorable effects on C_{l_β} to $\alpha = 25°$; however, C_{l_β} becomes unstable for angles of attack between 22° and 37°.

Finally, a third approach for further improvements in directional stability was suggested by the fact that the vortex system trailing from the fuselage-wing juncture on the windward side in sideslip actually produces a proverse flow field in the region above the vertical tail for a range of poststall angles of attack. Consequently, several vertical-tail extensions were tested, and the most acceptable compromise in terms of maximum effectiveness for a minimum increase in tail height is shown in the sketch in figure 7(c). The results of tests showing the effects of the vertical-tail extension on C_{n_β} and C_{l_β} are presented in figure 26. As expected, levels of directional stability are increased throughout the lower angle-of-attack range with the vertical-tail extension, and the angle of attack at which directional stability is lost is increased to greater than 17°. The effects on C_{l_β} are smaller than the effects produced by the leading-edge droop or the glove strake and the dihedral effect is lost between $\alpha = 19°$ and 26°.

In order to determine to what extent the beneficial effects produced by these modifications are additive, tests were conducted to determine their combined effects. A comparison of the combined effects of the droop and glove strake and of the droop, glove strake, and vertical-tail extension on C_{n_β} and C_{l_β} is presented in figure 27. These results indicate that the effects are generally additive. The angle of attack at which directional stability is lost is increased to greater than 17° with the droop and glove strake, and C_{l_β} is maintained at moderate levels up to an angle of attack of about 26°. Addition of the vertical-tail extension improves directional stability over the lower angle-of-attack range and increases the angle of attack at which directional stability becomes zero to greater than 20°, an increase of about 6° over the unmodified configuration. Also, a small additional increase in effective dihedral is noted.

The effects of the modified wing-leading- and trailing-edge sections on levels of C_{n_β} and C_{l_β} for the basic configuration and for the configuration modified with droop, glove strake, and vertical-tail

extension are presented in figures 28 and 29. respectively. The results indicate that the modified wing sections generally have small effects on the static lateral-directional characteristics of the configurations.

The combined effects of all the modifications on C_{n_β} and C_{l_β} are shown for the cruise configuration and for the takeoff–powered approach configuration in figures 30(a) and 30(b). The combined effects for the cruise configuration are considered to be very significant. The directional stability is improved over the lower angle-of-attack range and the angle of attack at which directional stability is lost is increased 6° over that of the basic configuration. In addition, the modified configuration remains laterally stable well beyond stall. For the takeoff–powered approach configuration some improvement is noted in levels of C_{n_β} and C_{l_β} up to an angle of attack of 22°. The angle of attack at which directional stability becomes zero increased from about 18° to above 20°.

Roll control augmentation. As noted previously, the airplane exhibits a marked reduction in lateral control near stall. Therefore, one of the objectives of the study was to investigate ways to maintain adequate levels of lateral control beyond stall. Deflecting the existing speed-brake panels as ailerons (see fig. 9) was explored as a method for augmenting the flaperon roll control. Test results showing available roll control with maximum flaperon deflection ($\delta_f = 51°$) and with combined flaperon and speed-brake deflection are presented in figure 31 for the cruise configuration. These results indicate that substantial additional roll control is available by deflecting both upper and lower speed-brake panels up on one wing and both panels down on the other wing. With this arrangement, roll control is maintained beyond maximum trim angles of attack at about 30 percent of the maximum roll control with flaperon deflection only.

Results of $C_{n_{\beta,\mathrm{dyn}}}$ Calculations

Previous investigators have shown that positive values of the dynamic stability parameter $C_{n_{\beta,\mathrm{dyn}}}$ at high angles of attack indicate a resistance to directional divergence. (See, for instance, ref. 9.) A description of the derivation of this parameter can be found in reference 10. Values of $C_{n_{\beta,\mathrm{dyn}}}$ calculated from the static wind-tunnel data discussed previously are shown in figure 32 for the basic and modified configurations.

Basic configuration. The data for the unmodified cruise configuration (fig. 32(a)) show that $C_{n_{\beta,\mathrm{dyn}}}$ approaches zero at an angle of attack of about 16°. This angle of attack is near the value at which C_{n_β} and C_{l_β} approach zero. (See fig. 17(a).) For the purpose of illustration, the angle of attack corresponding to a $2g$ maneuver (ref. 4) is indicated in figure 32(a). This angle of attack (approximately 12°) corresponds to a 60° banked turn at an airspeed of 250 knots with the airplane at a weight of 47 500 lb. A comparison of this angle of attack with that at which $C_{n_{\beta,\mathrm{dyn}}}$ becomes zero indicates an angle-of-attack margin of about 4° before departure resistance is lost.

The data for the unmodified takeoff–powered approach configuration (fig. 32(b)) show that $C_{n_{\beta,\mathrm{dyn}}}$ approaches zero at an angle of attack of about 20°. In contrast with the cruise configuration, however, $C_{n_{\beta,\mathrm{dyn}}}$ is positive for angles of attack to 30° except for a small region at $\alpha \approx 20°$.

Modified configuration. The combined effects of the modifications on $C_{n_{\beta,\mathrm{dyn}}}$ are also shown in figure 32 for the cruise configuration and the takeoff–powered approach configuration. These data include the combined effects of the leading-edge droop, glove strake, vertical-tail extension, and modified wing-leading- and trailing-edge sections. For the modified cruise configuration (fig. 32(a)) $C_{n_{\beta,\mathrm{dyn}}}$ remains positive to an angle of attack of about 23°, about a 7° increase over that of the unmodified configuration. For the modified takeoff powered approach configuration (fig. 32(b)) $C_{n_{\beta,\mathrm{dyn}}}$ remains positive to angles of attack greater than 30°, largely because of the more negative value of C_{l_β} afforded by the modifications at an angle of attack of about 24°. (See fig. 30(b).)

The results indicate that these modifications significantly improve the dynamic lateral-directional behavior of both the cruise and takeoff–powered approach configurations. For example, for the modified cruise configuration the increase in angle of attack for which $C_{n_{\beta,\mathrm{dyn}}}$ remains positive represents about a 175-percent increase in the angle-of-attack margin over that of the unmodified configuration for the $2g$ maneuver discussed previously.

Results and Discussion of Free-Flight Tests

The free-flight tests were conducted to determine the dynamic stability and control characteristics of the basic and modified model configurations, with emphasis on the effectiveness of the model geometry and control-system modifications in preventing or delaying to a higher angle of attack the occurrence of lateral-directional divergence problems. The results

consist mainly of qualitative pilot observations and opinions of the behavior of the model. Quantitative data are presented in the form of time histories of pilot control inputs, model angle of attack, and angular rates.

Longitudinal Characteristics

Because the primary objective of the free-flight tests was to study lateral-directional stability and control characteristics, the pitch stability augmentation system (SAS) was maintained at a higher than normal level for all flights to provide longitudinal steadiness and smooth flight conditions for easier evaluation of the lateral-directional flight characteristics. For all flights the pitch SAS gain was maintained at an increased level ($K_q = 0.5$) instead of the nominal value ($K_q = 0.0412$). Stability augmentation provided by the pitch-rate signal driving the all-movable horizontal tail gave the model good longitudinal characteristics throughout the test angle-of-attack range. The task of the pitch pilot was simply to maintain steady flight at the desired location in the test section so that lateral-directional piloting tasks could be conducted as effectively as possible.

Lateral-Directional Characteristics

Cruise configuration. Because of the high tunnel speeds necessary for flight of the cruise configuration and because of the high angular rates of the model due to its relatively small scale (1/8.5), safety considerations required that the high-angle-of-attack gains be used for all flights of this configuration. Also, during the free-flight test the basic cruise configuration exhibited weak roll control that required a high pilot work load to control the model, even with the use of the speed brakes to augment roll control.

The rudder remained effective for maintaining directional control, for controlling yaw disturbances, and for generating sideslip to provide a rolling moment through the dihedral effect to help keep the wings level. One of the problems with flying the basic cruise configuration at the higher angles of attack was a tendency for one wing to drop because of intermittent asymmetric wing stalling, low roll damping, and tunnel gustiness. The flaperon control effectiveness deteriorated rapidly with increasing angle of attack and became ineffective for roll control or for providing artificial roll damping as wing stall occurred. The use of the wing-tip speed brake provided some additional roll control, which was beneficial at the higher angles of attack. A very high pilot work load was required to keep the model under control and to sustain smooth flights as the angle of attack was increased beyond 17°. By applying constant attention to the controls, the pilot could manage sustained flight up to an angle of attack of about 21°. At $\alpha = 21°$, the model exhibited a lateral-directional divergence against full corrective control. Values of $C_{n_{\beta,\mathrm{dyn}}}$ calculated with β feedback to the rudder and flaperon are shown in figure 33. This is done by calculating $C_{n_{\beta,\mathrm{dyn}}}$ with the augmented values of C_{n_β} and C_{l_β}, which are defined as follows:

$$C_{n_{\beta,\mathrm{aug}}} = C_{n_\beta} K_{Y,\beta} C_{n_{\delta_r}}$$

$$C_{l_{\beta,\mathrm{aug}}} = C_{l_\beta} K_{R,\beta} C_{l_{\delta_f}}$$

Comparison of the flight-test results for the basic cruise configuration with values of $C_{n_{\beta,\mathrm{dyn}}}$ calculated with the augmented lateral-directional derivatives shows good agreement for the departure angle of attack.

The addition of the airframe modifications (leading-edge glove strake, inboard wing-leading-edge droop, vertical-tail extension, and modified wing-leading-edge and trailing-edge sections) improved the lateral-directional stability of the model such that sustained flights could be made up to an angle of attack of 27°. At this angle of attack a loss in lift and a yaw departure caused the flight to be terminated. The primary benefit of the modifications appears to be in improved C_{n_β} and C_{l_β}, as indicated in figure 30(a). In figure 30(a) C_{n_β} and C_{l_β} for the modified configuration approach the same values as those for the basic configuration at about $\alpha = 27°$. A comparison of the free-flight results with the $C_{n_{\beta,\mathrm{dyn}}}$ data of figure 33 shows generally good agreement for the angle of attack at which the modified configuration departed and that estimated based on the change in sign of $C_{n_{\beta,\mathrm{dyn}}}$ from positive to negative.

Figure 34 presents time histories of flights made with the basic and modified configurations. The large roll stick inputs required to control the model and the large roll excursions prior to departure are apparent for the basic configuration. With the modified configuration, smooth sustained flights were possible with much less pilot effort than that noted for the unmodified cruise configuration. In addition, the roll damping of the modified configuration was more stable than that for the basic configuration, and this stability contributed significantly to the improved flight behavior of this configuration. Limited flight tests made with the β-feedback turned off showed a marked deterioration in the high-angle-of-attack flight characteristics of the model, and sustained flights were difficult beyond an angle of attack of about 20°.

Takeoff–powered approach configuration. Flight tests of the basic takeoff–powered approach configuration also required the use of the high-angle-of-attack control system to provide the best flight behavior. One of the obvious flight characteristics was a rolling oscillation that was associated with a loss of roll damping at high angles of attack. The piloting task increased in difficulty with increasing angle of attack and was aggravated by deterioration in flaperon effectiveness at the higher angles of attack. Flights with flaperons alone were difficult above $\alpha = 14°$. This loss in flaperon effectiveness made it difficult to provide coordinated lateral-directional control, and smooth sustained flights required an increased roll gain to avoid pilot-induced roll oscillation from rudder control. As angle of attack increased to 20°, the model experienced an uncontrollable lateral-directional divergence. This divergence was characterized primarily by a roll-off followed by a yaw departure. Comparison of the free-flight results with the $C_{n_{\beta,\mathrm{dyn}}}$ data of figure 32(b) shows good agreement between the measured departure angle and the predicted departure angle based on the change in sign of $C_{n_{\beta,\mathrm{dyn}}}$.

The addition of the airframe modifications provided beneficial effects similar to those observed for the cruise configuration. The modifications provided improvements in lateral-directional stability that made sustained flights possible up to an angle of attack of 24°. At this angle of attack the model experienced a departure that was characterized primarily by a roll divergence that appeared to be brought on by loss of roll damping and loss of lateral control. The departure angle of attack of 24° is in disagreement with the $C_{n_{\beta,\mathrm{dyn}}}$ data in figure 32(b), which shows positive values of $C_{n_{\beta,\mathrm{dyn}}}$ to higher angles of attack. This disagreement is associated with the fact that the divergence was characterized more by a rolling departure brought on by possible losses of roll damping and lateral control rather than by a more typical directional divergence. In any event, the free-flight test results confirm the static force test data as far as the benefits of the modifications on lateral-directional characteristics are concerned. They show that the modifications provide an improvement in departure angle of attack of about 4° for the takeoff-powered approach configuration and an improvement of 6° for the cruise configuration.

Concluding Remarks

The results of a static and free-flight wind-tunnel investigation of the high-angle-of-attack stability and control characteristics of a model of the EA-6B airplane configuration indicate the following conclusions:

1. The static force tests showed that the unmodified configuration experiences a loss of directional stability and a loss of effective dihedral at high angles of attack. Flow-visualization studies indicate that the loss of directional stability results from an adverse (destabilizing) sidewash at the aft fuselage and vertical-tail location that is produced by a vortex system originating near the fuselage-wing juncture. The loss of effective dihedral is related to a combination of stalling of the leading wing panel at high angles of attack and the effect of the adverse sidewash on the vertical tail.

2. An inboard wing-leading-edge droop, a glove strake, and a vertical-tail extension, when combined, significantly improve the static lateral-directional stability of the configuration. The computationally designed modifications for the wing slat and flap sections (intended for performance benefits) do not appreciably affect the lateral-directional stability characteristics at the Reynolds numbers of these tests. Deflecting the existing speed-brake panels (as ailerons) in conjunction with the flaperons significantly improves roll control.

3. In the free-flight tests the unmodified cruise configuration experienced a lateral-directional divergence against full corrective control. The unmodified takeoff–powered approach configuration experienced a lateral-directional departure that was characterized by a roll-off followed by a yaw departure. The results of the free-flight tests confirm the trends indicated by static force test data, which show a loss of directional and lateral stability at high angles of attack. The model with the airframe modifications and with high-angle-of-attack stability augmentation exhibits good dynamic stability characteristics and can be flown at significantly higher angles of attack than the unmodified configuration. These results generally correlate well with predictions from calculated values of dynamic stability parameter $C_{n_{\beta,\mathrm{dyn}}}$.

NASA Langley Research Center
Hampton, VA 23665-5225
March 5, 1992

References

1. Hanley, Robert J.: Development of an Airframe Modification To Improve the Mission Effectiveness of the EA-6B Airplane. *A Collection of Technical Papers AIAA 5th Applied Aerodynamics Conference*, Aug. 1987, pp. 241 247. (Available as AIAA-87-2358.)

2. Sewall, W. G.; McGhee, R. J.; and Ferris, J. C.: Wind-Tunnel Test Results of Airfoil Modifications for the EA-6B. *A Collection of Technical Papers AIAA 5th Applied Aerodynamics Conference*, Aug. 1987, pp. 248 256. (Available as AIAA-87-2359.)

3. Waggoner, E. G.; and Allison, D. O.: EA-6B High-Lift Wing Modifications. *A Collection of Technical Papers AIAA 5th Applied Aerodynamics Conference*, Aug. 1987, pp. 257 269. (Available as AIAA-87-2360.)

4. Gato, W.; and Masiello, M. F.: Innovative Aerodynamics: The Sensible Way of Restoring Growth Capability to the EA-6B Prowler. *A Collection of Technical Papers AIAA 5th Applied Aerodynamics Conference*, Aug. 1987, pp. 286 299. (Available as AIAA-87-2362.)

5. Allison, Dennis O.; and Waggoner, E. G.: *Prediction of Effects of Wing Contour Modifications on Low-Speed Maximum Lift and Transonic Performance for the EA-6B Aircraft*. NASA TP-3046, 1990.

6. Chambers, Joseph R.; Bowman, James S., Jr.; and Malcolm, Gerald N.: Stall/Spin Test Techniques Used by NASA. *Stall/Spin Problems of Military Aircraft*, AGARD-CP-199, June 1976, pp. 13-1 13-12.

7. Wolowicz, Chester H.; Bowman, James S., Jr.; and Gilbert, William P.: *Similitude Requirements and Scaling Relationships as Applied to Model Testing*. NASA TP-1435, 1979.

8. Polhamus, Edward C.; and Spreeman, Kenneth P.: *Subsonic Wind-Tunnel Investigation of the Effect of Fuselage Afterbody on Directional Stability of Wing-Fuselage Combinations at High Angles of Attack*. NACA TN 3896, 1956.

9. Chambers, Joseph R.; and Anglin, Ernie L.: *Analysis of Lateral-Directional Stability Characteristics of a Twin-Jet Fighter Airplane at High Angles of Attack*. NASA TN D-5361, 1969.

10. Moul, Martin T.; and Paulson, John W.: *Dynamic Lateral Behavior of High-Performance Aircraft*. NACA RM L58E16, 1958.

Table I. Model Mass and Geometric Characteristics

Weight, lb	86.0
Moments of inertia:	
I_X, slug-ft^2	2.83
I_Y, slug-ft^2	5.78
I_Z, slug-ft^2	8.08
Overall length, ft	6.99
Wing:	
Span, ft	6.24
Reference area (excluding fillets), ft^2	7.320
Root chord, ft	1.79
Tip chord, ft	0.56
Mean aerodynamic chord, ft	1.28
Aspect ratio	5.310
Taper ratio	0.312
Sweepback of 0.25c, deg	25.00
Dihedral (outboard of W.S. 7.65)	−1.00
Incidence, deg	0
Airfoil section:	
W.S. 3.88	NACA 64A009 (modified)
Tip	NACA 64A005.9 (modified)
Flaperon area (one side), ft^2	0.307
Flaperon span (from 20.44 percent $b/2$ to 85.66 percent $b/2$), ft	2.03
Flap area (one side), ft^2	0.720
Leading-edge slat area (one side), ft^2	0.345
Speed-brake area (wing tip one side), ft^2	0.221
Horizontal tail:	
Area, ft^2	1.619
Span, ft	2.39
Aspect ratio	3.530
Taper ratio	0.405
Sweepback of 25-percent chord, deg	30.00
Dihedral, deg	0
Root chord, ft	0.97
Tip chord, ft	0.39
Airfoil section:	
Root	66A009 (modified)
Tip	64A007 (modified)
Vertical tail:	
Area including radome, ft^2	1.206
Aspect ratio	0.962
Taper ratio	0.307
Root chord, ft	1.62
Tip chord, ft	0.50
Sweepback of 25-percent chord, deg	28.00
Airfoil section:	
Root	64A008.1 (modified)
Tip	64A006.5 (modified)
Rudder area, ft^2	0.226

Table II. Airfoil Coordinates of Basic Wing

(a) Inboard design station, W.S. 10.35 in.

x/c	$(z/c)_u$	$(z/c)_l$
0.00000	0.00041	0.00041
.00100	.00380	−.00240
.00300	.00661	−.00433
.00500	.00847	−.00562
.00700	.00995	−.00659
.01000	.01184	−.00774
.02000	.01673	−.01010
.03000	.02065	−.01160
.04000	.02403	−.01281
.05000	.02702	−.01384
.06000	.02973	−.01473
.08000	.03443	−.01627
.10000	.03839	−.01763
.12000	.04179	−.01890
.14000	.04471	−.02011
.16000	.04721	−.02129
.18000	.04933	−.02243
.20000	.05119	−.02353
.25000	.05451	−.02613
.30000	.05633	−.02834
.35000	.05688	−.02999
.40000	.05623	−.03088
.45000	.05453	−.03091
.50000	.05186	−.03014
.55000	.04830	−.02866
.60000	.04406	−.02661
.65000	.03926	−.02397
.70000	.03400	−.02090
.75000	.02843	−.01749
.80000	.02283	−.01408
.82000	.02059	−.01271
.84000	.01835	−.01135
.86000	.01611	−.00998
.88000	.01387	−.00862
.90000	.01163	−.00725
.92000	.00939	−.00588
.94000	.00715	−.00452
.95000	.00603	−.00384
.96000	.00490	−.00315
.97000	.00378	−.00247
.98000	.00266	−.00179
.99000	.00154	−.00111
1.00000	.00042	−.00042

Table II. Concluded

(b) Outboard design station, W.S. 28.24 in.

x/c	$(z/c)_u$	$(z/c)_l$
0.00000	−0.00263	−0.00263
.00100	.00101	−.00464
.00300	.00320	−.00621
.00500	.00483	−.00720
.00700	.00613	−.00796
.01000	.00785	−.00882
.02000	.01252	−.01052
.03000	.01627	−.01135
.04000	.01948	−.01199
.05000	.02227	−.01251
.06000	.02481	−.01295
.08000	.02933	−.01363
.10000	.03315	−.01430
.12000	.03645	−.01499
.14000	.03925	−.01568
.16000	.04161	−.01640
.18000	.04360	−.01712
.20000	.04527	−.01787
.25000	.04834	−.01979
.30000	.05005	−.02158
.35000	.05053	−.02303
.40000	.04992	−.02403
.45000	.04834	−.02436
.50000	.04588	−.02380
.55000	.04265	−.02268
.60000	.03882	−.02118
.65000	.03455	−.01924
.70000	.02999	−.01686
.75000	.02529	−.01432
.80000	.02051	−.01172
.82000	.01858	−.01066
.84000	.01663	−.00960
.86000	.01469	−.00853
.88000	.01274	−.00746
.90000	.01079	−.00639
.92000	.00884	−.00532
.94000	.00689	−.00425
.95000	.00591	−.00372
.96000	.00494	−.00318
.97000	.00397	−.00265
.98000	.00300	−.00212
.99000	.00203	−.00159
1.00000	.00107	−.00107

Table III. Airfoil Coordinates of Wing With Modified Leading- and Trailing-Edge Sections

(a) Inboard design station, W.S. 10.35 in.

x/c	$(z/c)_u$	$(z/c)_l$
0.00000	0.00049	0.00049
.00100	.00497	−.00378
.00300	.00828	−.00657
.00500	.01053	−.00821
.00700	.01229	−.00931
.01000	.01441	−.01046
.02000	.01952	−.01251
.03000	.02335	−.01362
.04000	.02652	−.01442
.05000	.02924	−.01508
.06000	.03162	−.01565
.08000	.03569	−.01672
.10000	.03912	−.01782
.12000	.04212	−.01896
.14000	.04480	−.02013
.16000	.04721	−.02129
.18000	.04933	−.02243
.20000	.05119	−.02353
.25000	.05451	−.02613
.30000	.05633	−.02834
.35000	.05688	−.02999
.40000	.05623	−.03088
.45000	.05453	−.03091
.50000	.05186	−.03014
.55000	.04830	−.02866
.60000	.04406	−.02661
.65000	.03926	−.02397
.70000	.03400	−.02088
.75000	.02843	−.01695
.80000	.02283	−.01162
.82000	.02063	−.00900
.84000	.01846	−.00614
.86000	.01635	−.00324
.88000	.01441	−.00062
.90000	.01268	.00151
.92000	.01111	.00298
.94000	.00968	.00358
.95000	.00903	.00345
.96000	.00846	.00296
.97000	.00798	.00209
.98000	.00762	.00078
.99000	.00740	−.00103
1.00000	.00735	−.00338

Table III. Concluded

(b) Outboard design station, W.S. 28.24 in.

x/c	$(z/c)_u$	$(z/c)_l$
0.00000	−0.00600	−0.00600
.00100	−.00193	−.00959
.00300	.00114	−.01168
.00500	.00323	−.01283
.00700	.00488	−.01356
.01000	.00695	−.01427
.02000	.01218	−.01526
.03000	.01621	−.01545
.04000	.01959	−.01539
.05000	.02252	−.01522
.06000	.02512	−.01504
.08000	.02959	−.01483
.10000	.03334	−.01490
.12000	.03654	−.01522
.14000	.03928	−.01574
.16000	.04162	−.01640
.18000	.04360	−.01712
.20000	.04527	−.01787
.25000	.04834	−.01979
.30000	.05005	−.02158
.35000	.05053	−.02303
.40000	.04992	−.02403
.45000	.04834	−.02436
.50000	.04588	−.02380
.55000	.04265	−.02268
.60000	.03882	−.02118
.65000	.03455	−.01924
.70000	.02999	−.01689
.75000	.02529	−.01384
.80000	.02051	−.00961
.82000	.01861	−.00750
.84000	.01673	−.00516
.86000	.01490	−.00279
.88000	.01320	−.00065
.90000	.01168	.00107
.92000	.01030	.00223
.94000	.00904	.00265
.95000	.00847	.00249
.96000	.00797	.00203
.97000	.00754	.00124
.98000	.00722	.00007
.99000	.00702	−.00152
1.00000	.00698	−.00359

Table IV. Airfoil Coordinates of Wing With Inboard Leading-Edge Droop

[Inboard design station, W.S. 10.35 in.]

x/c	$(z/c)_u$	$(z/c)_l$
−0.01965	−0.01287	−0.01287
−.01900	−.00963	−.01576
−.01700	−.00613	−.01836
−.01500	−.00384	−.01967
−.01300	−.00194	−.02059
−.01000	.00049	−.02156
.00000	.00692	−.02336
.01000	.01212	−.02418
.02000	.01673	−.02455
.03000	.02065	−.02459
.04000	.02403	−.02440
.05000	.02702	−.02407
.06000	.02973	−.02365
.08000	.03443	−.02262
.10000	.03839	−.02161
.12000	.04179	−.02074
.14000	.04471	−.02047
.16000	.04721	−.02129
.18000	.04933	−.02243
.20000	.05119	−.02353
.25000	.05451	−.02613
.30000	.05633	−.02834
.35000	.05688	−.02999
.40000	.05623	−.03088
.45000	.05453	−.03091
.50000	.05186	−.03014
.55000	.04830	−.02866
.60000	.04406	−.02661
.65000	.03926	−.02397
.70000	.03400	−.02088
.75000	.02843	−.01695
.80000	.02283	−.01162
.82000	.02063	−.00900
.84000	.01846	−.00614
.86000	.01635	−.00324
.88000	.01441	−.00062
.90000	.01268	.00151
.92000	.01111	.00298
.94000	.00968	.00358
.95000	.00903	.00345
.96000	.00846	.00296
.97000	.00798	.00209
.98000	.00762	.00078
.99000	.00740	−.00103
1.00000	.00735	−.00338

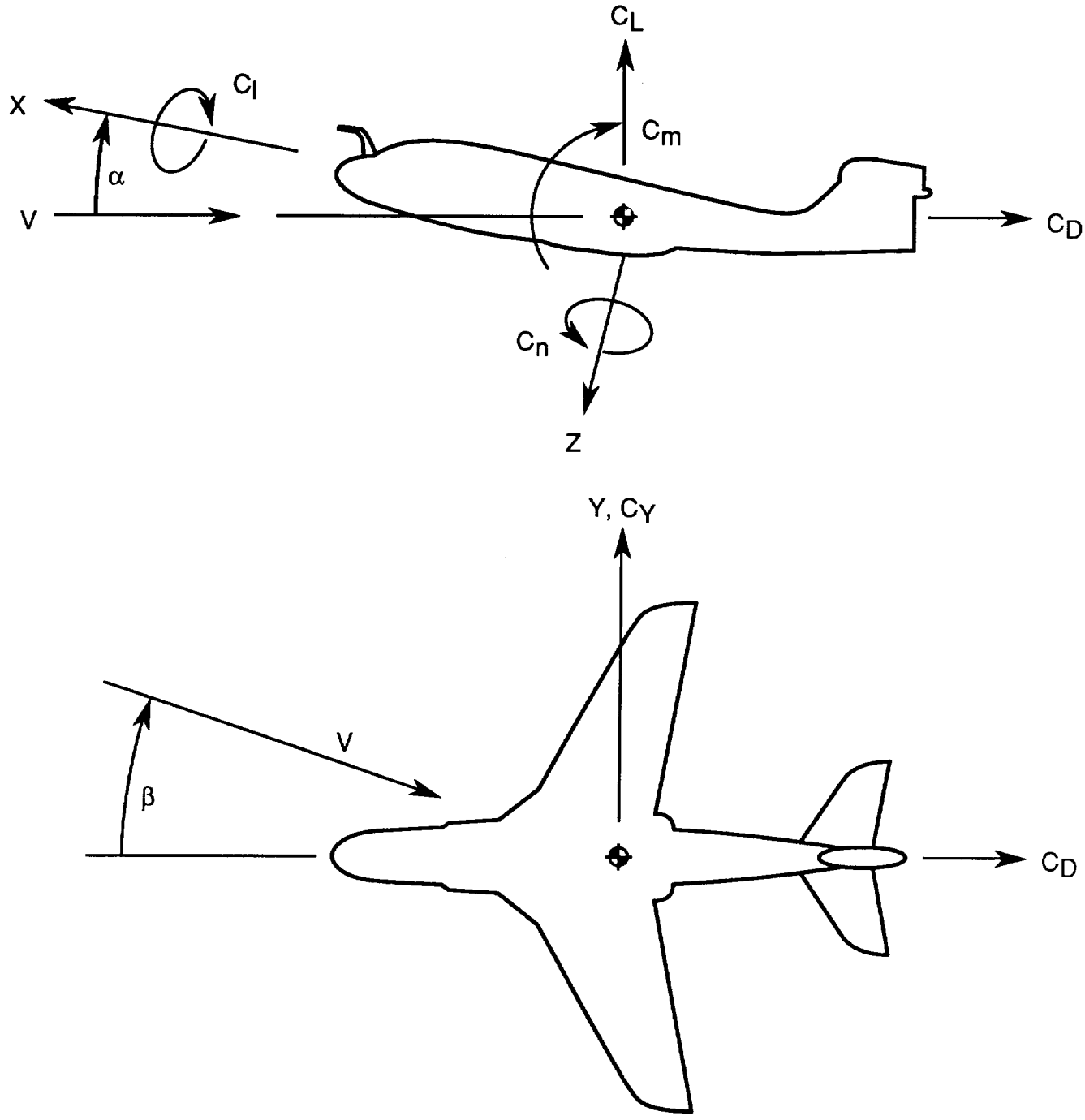

Figure 1. System of axes.

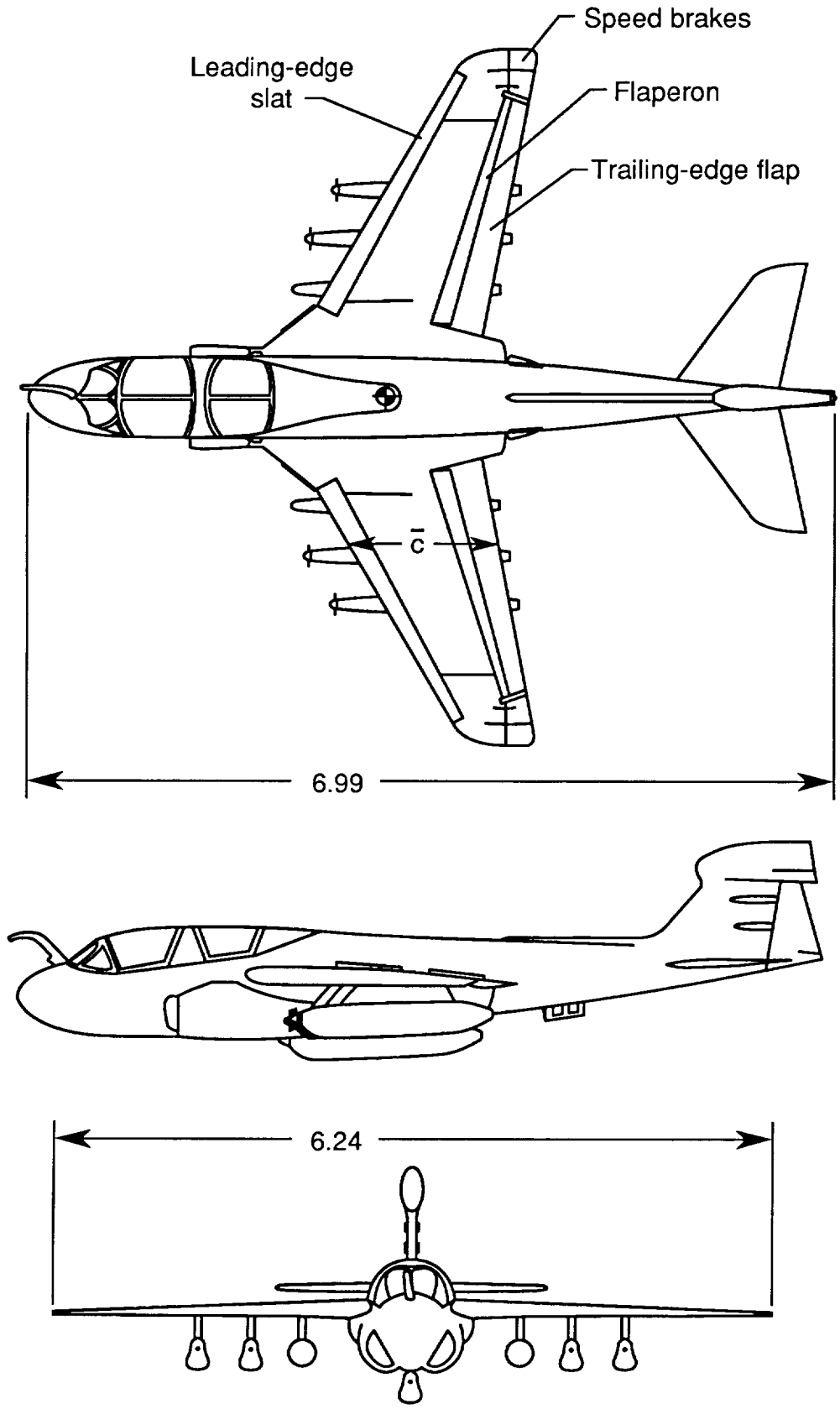

Figure 2. Three-view sketch of model airplane configuration. Dimensions are given in feet. $S = 7.32$ ft^2; $b = 6.24$ ft; $\bar{c} = 1.28$ ft; c.g. shown at $0.253\bar{c}$.

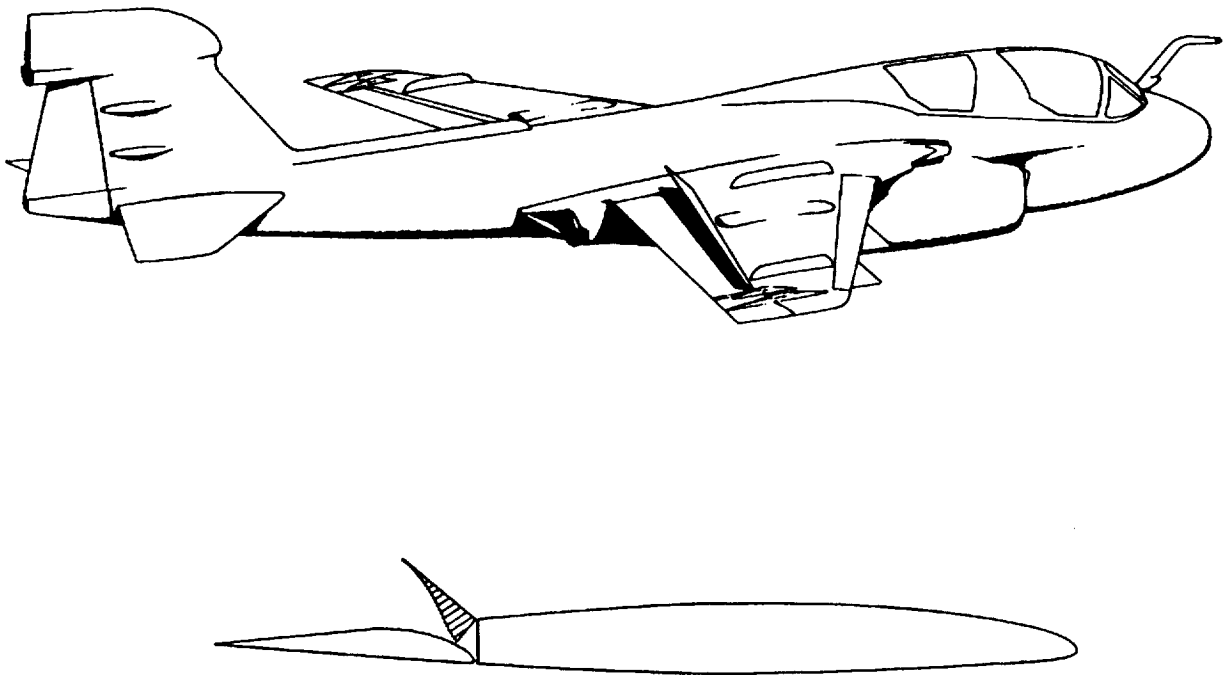

Figure 3. Sketch of deflected flaperon.

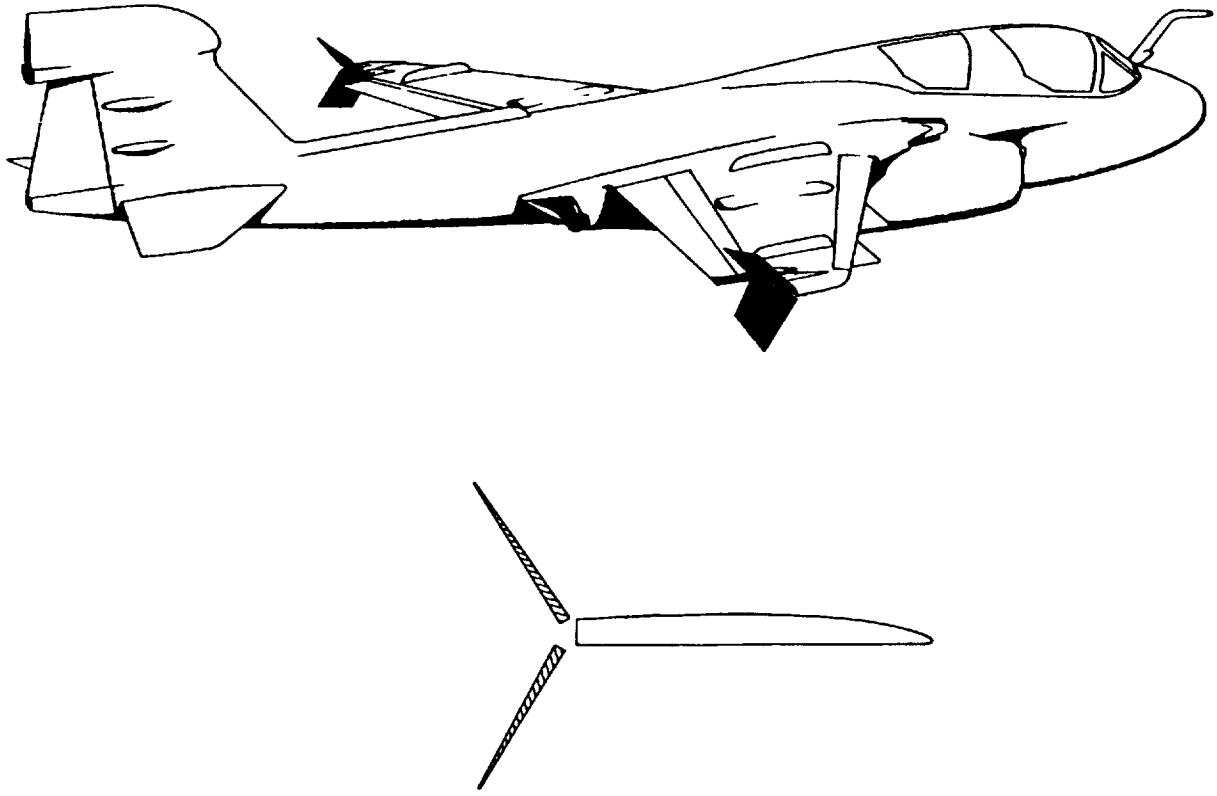

Figure 4. Sketch of speed brakes.

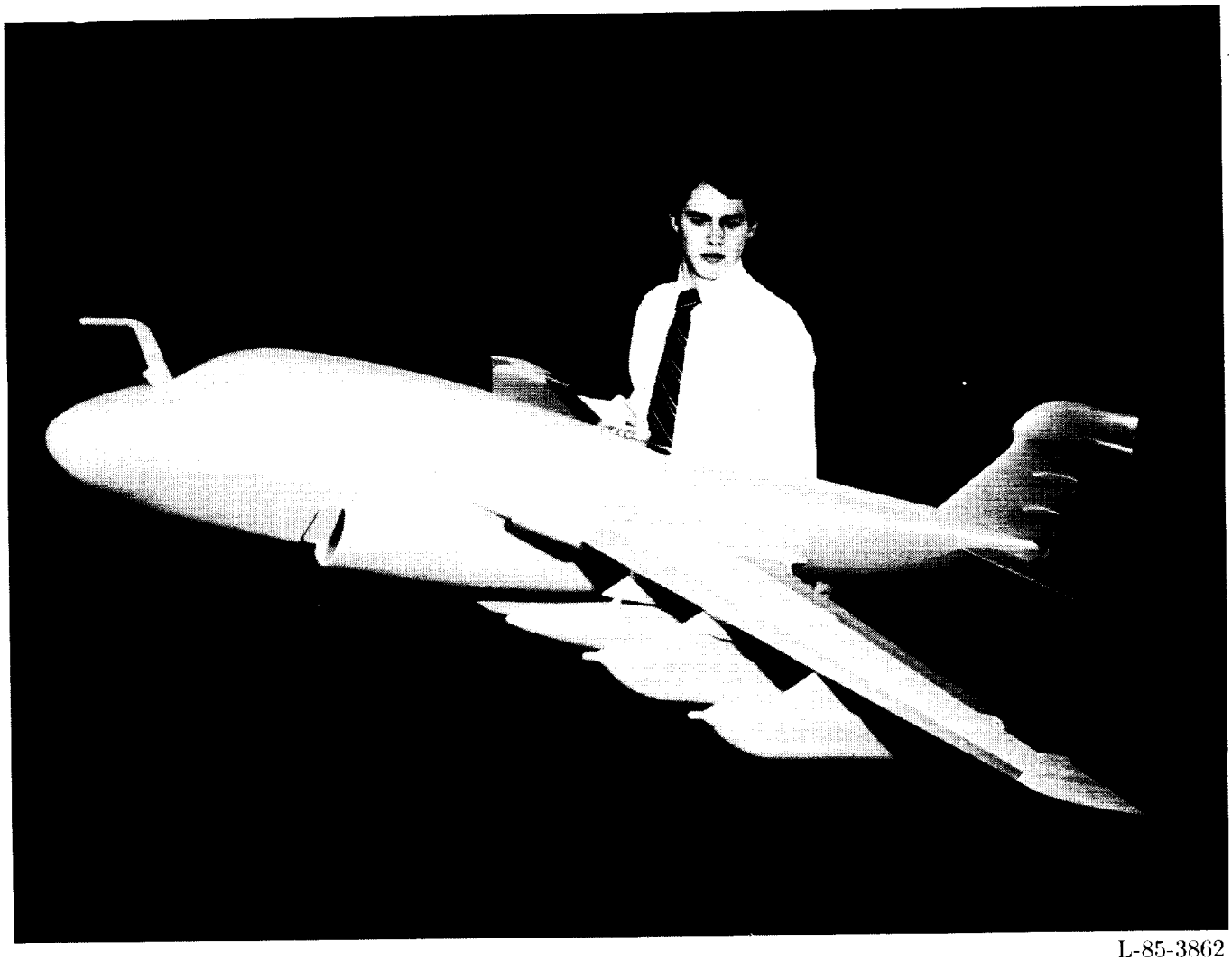

L-85-3862

Figure 5. Photograph of model.

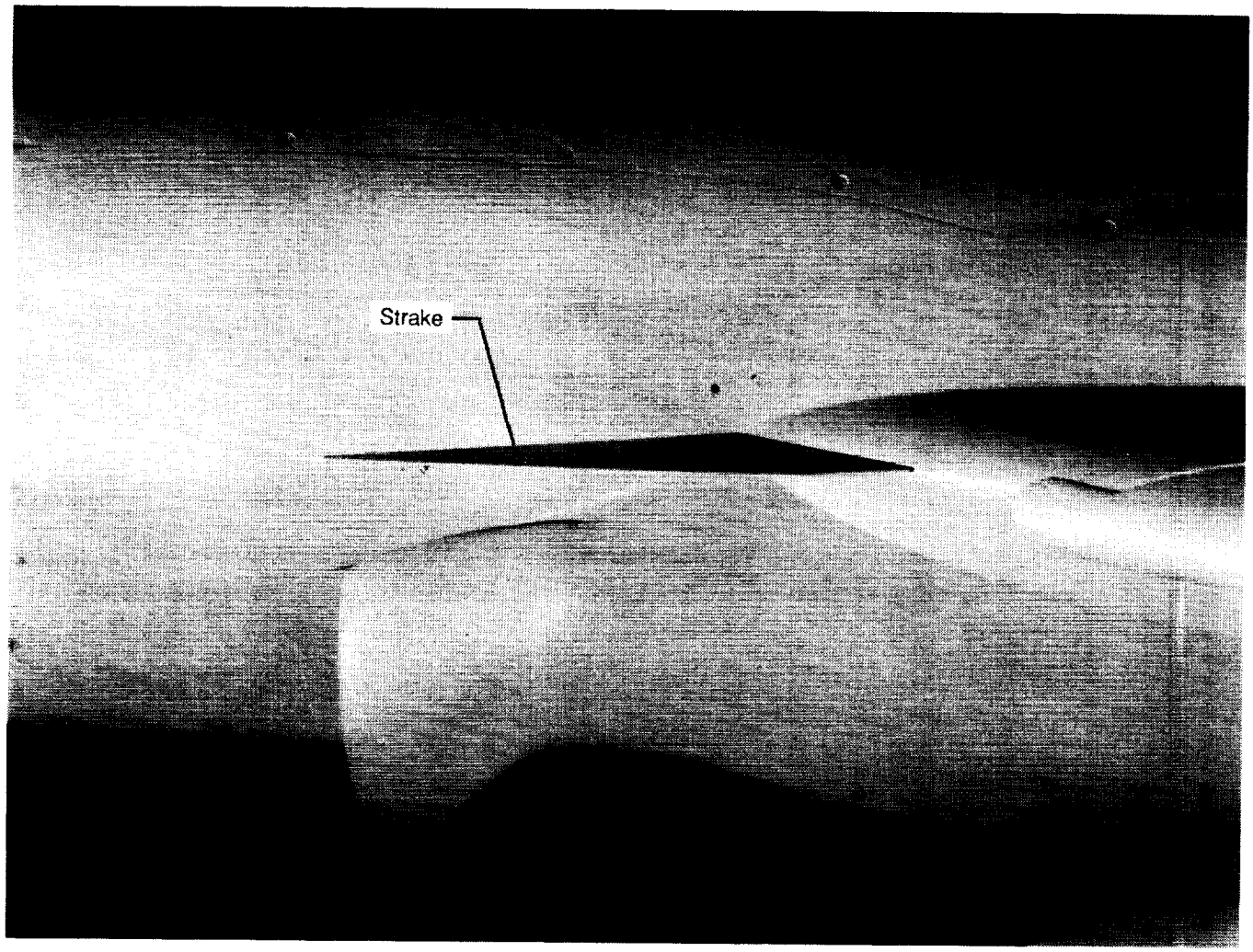

L-85-10882

(a) Glove leading-edge strake.

Figure 6. Airframe modifications for improved lateral-directional stability.

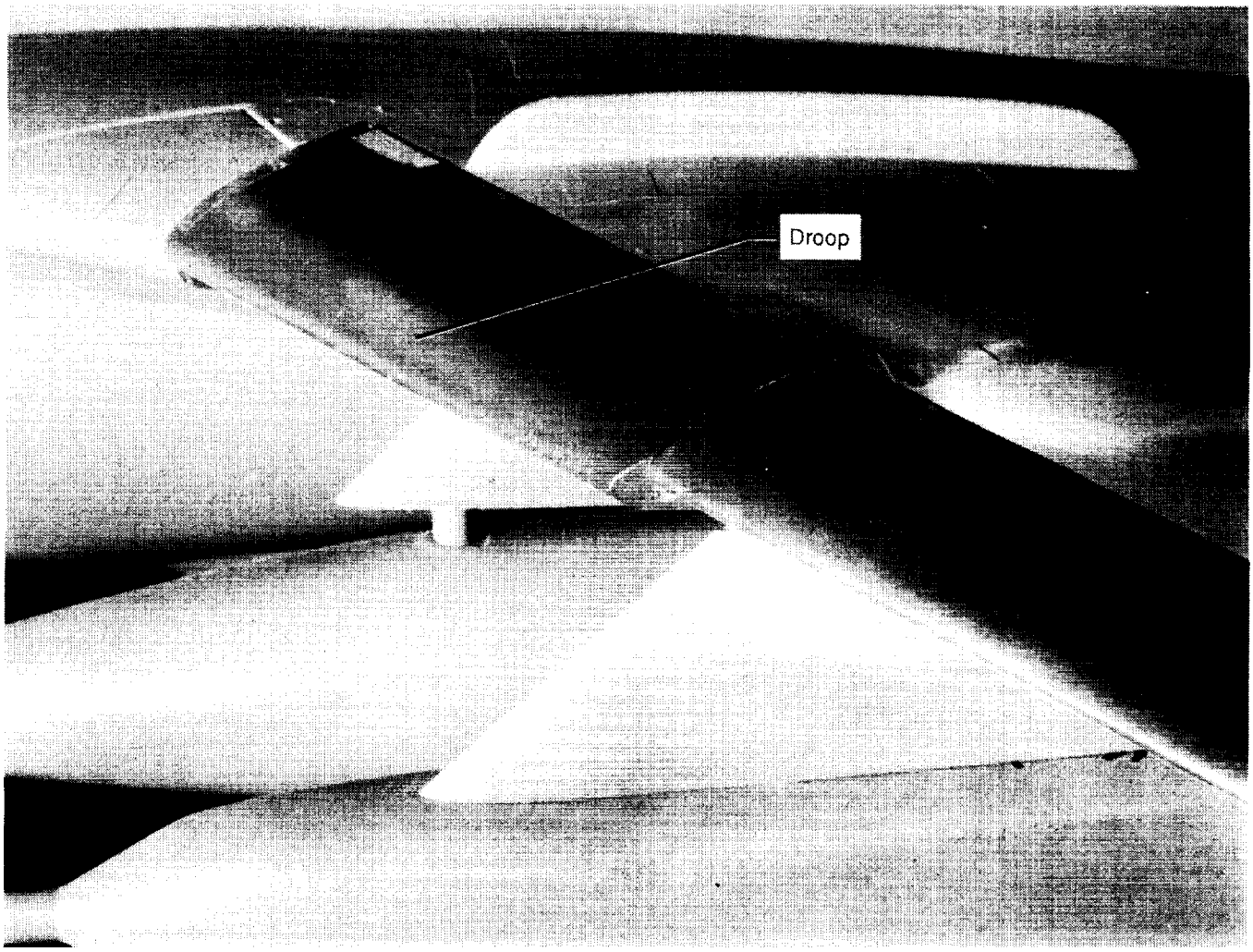

L-85-10883

(b) Inboard leading-edge droop.

Figure 6. Continued.

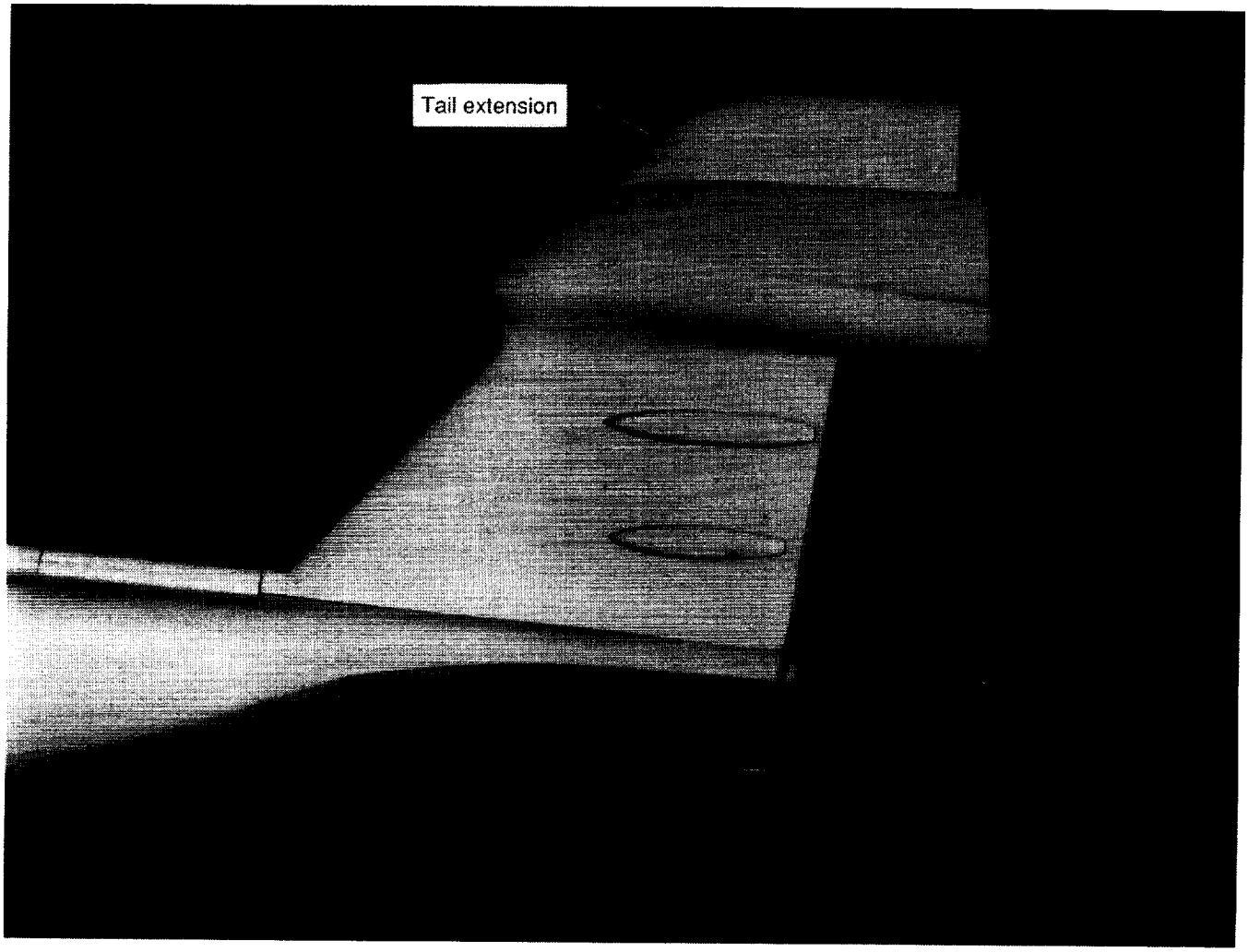

L-85-10886

(c) Vertical-tail extension.

Figure 6. Concluded.

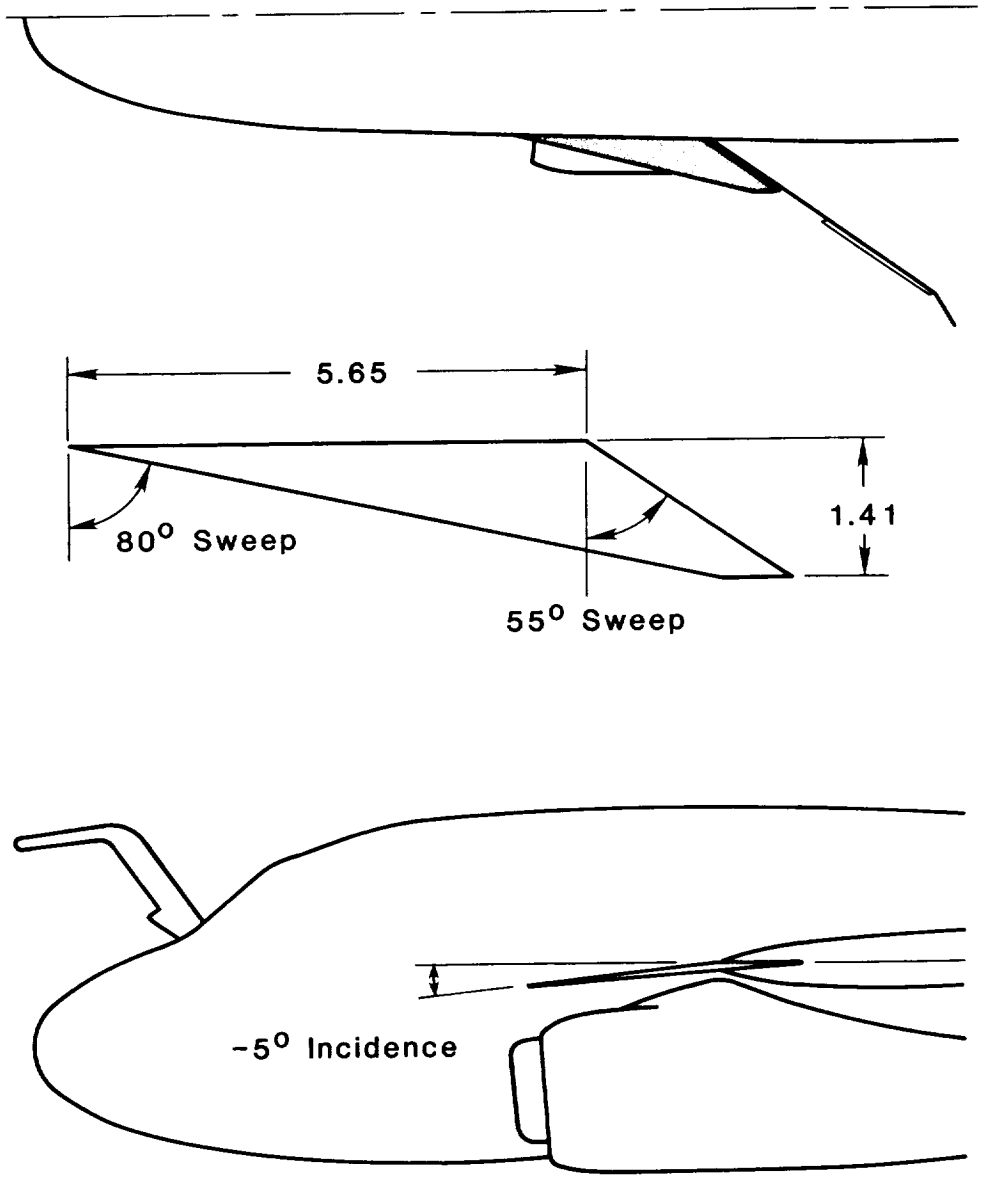

(a) Glove leading-edge strake.

Figure 7. Details of modifications. Model-scale dimensions are given in inches unless otherwise indicated.

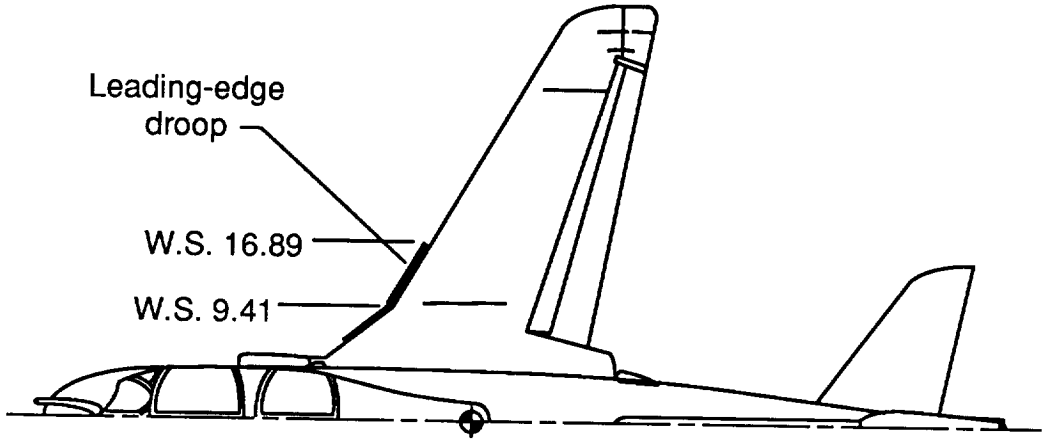

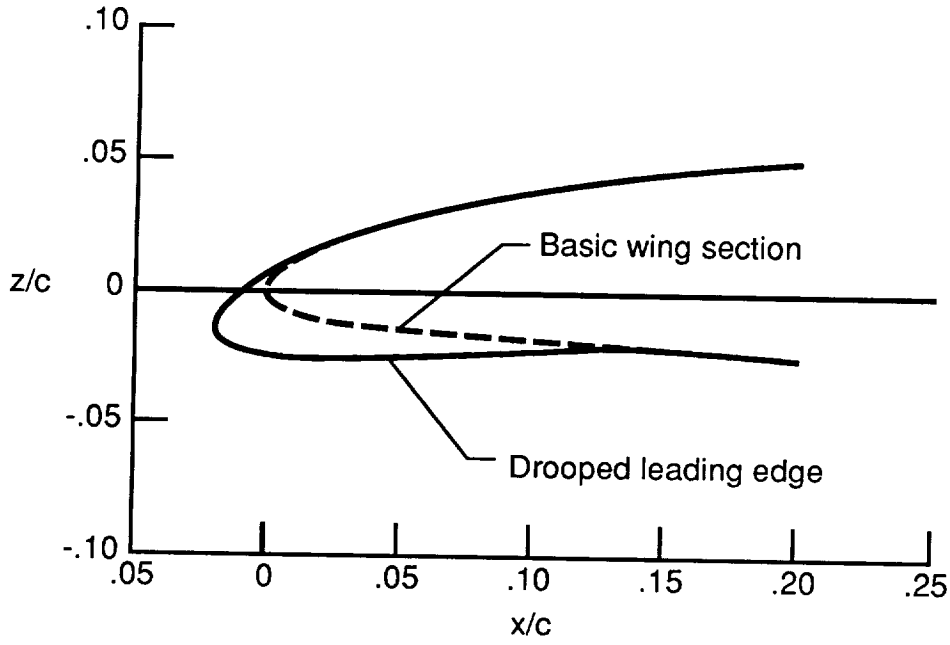

(b) Inboard leading-edge droop.

Figure 7. Continued.

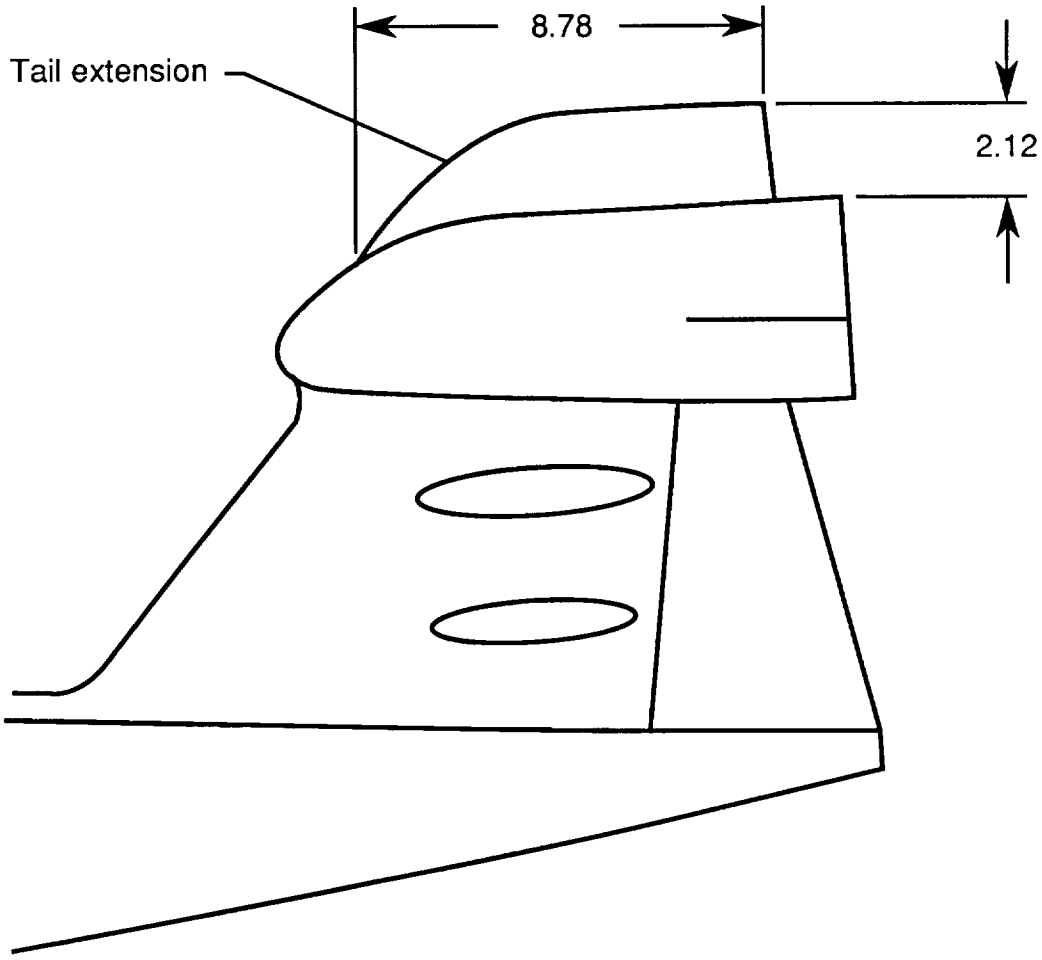

(c) Vertail-tail extension.

Figure 7. Concluded.

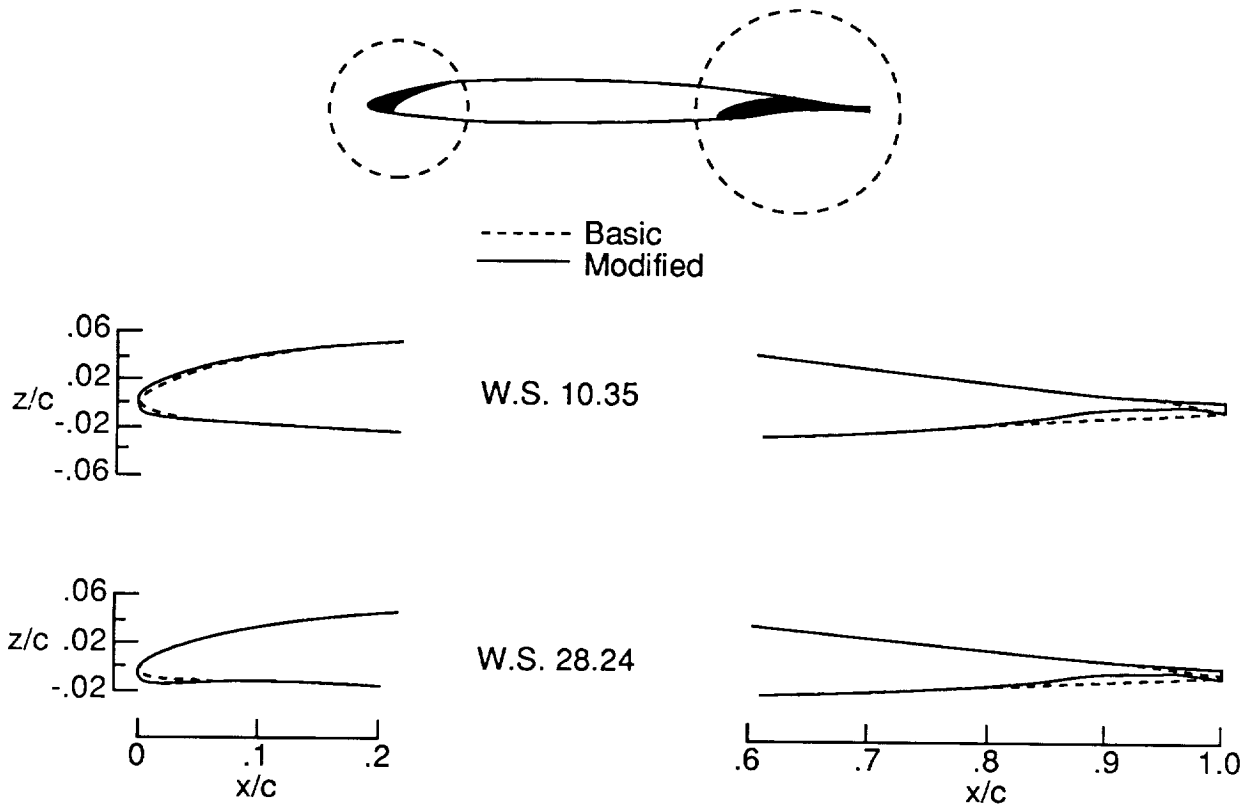

Figure 8. Modified leading- and trailing-edge sections. Model-scale wing stations are given in inches.

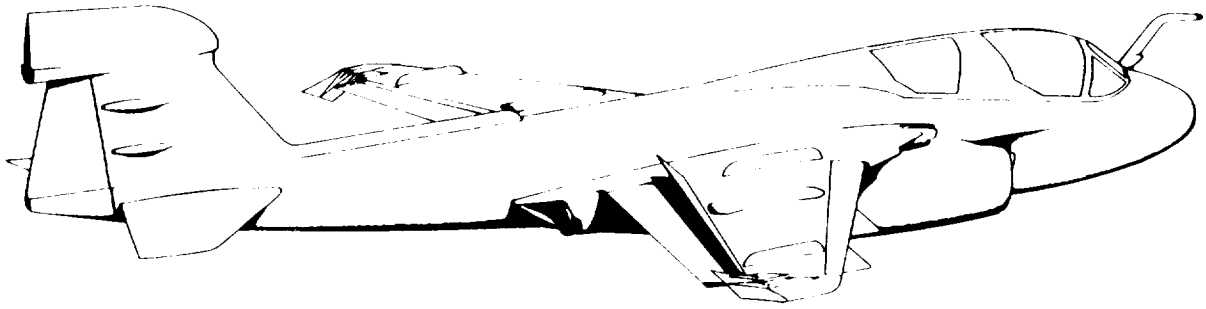

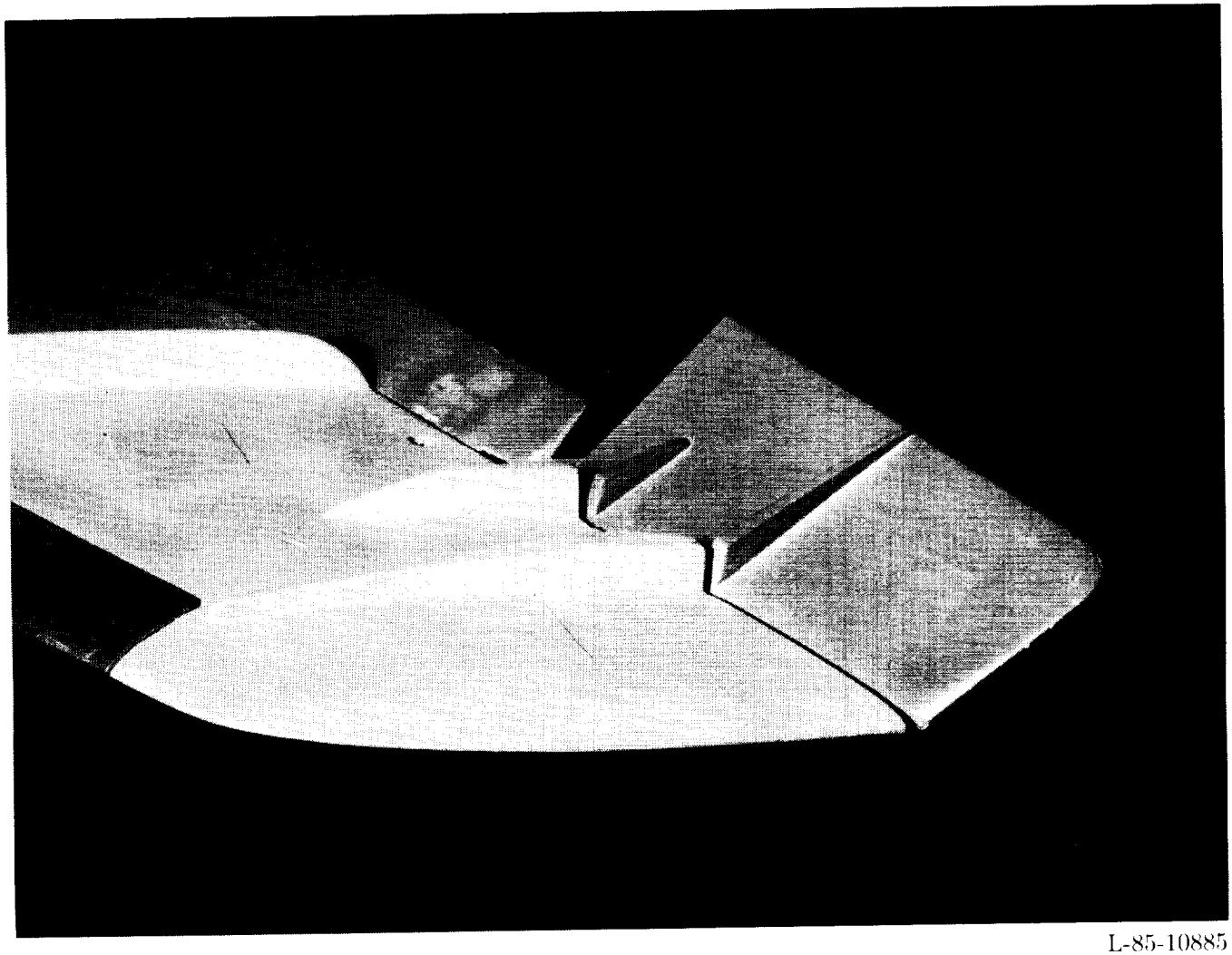

L-85-10885

Figure 9. Speed brake used as aileron for roll control augmentation.

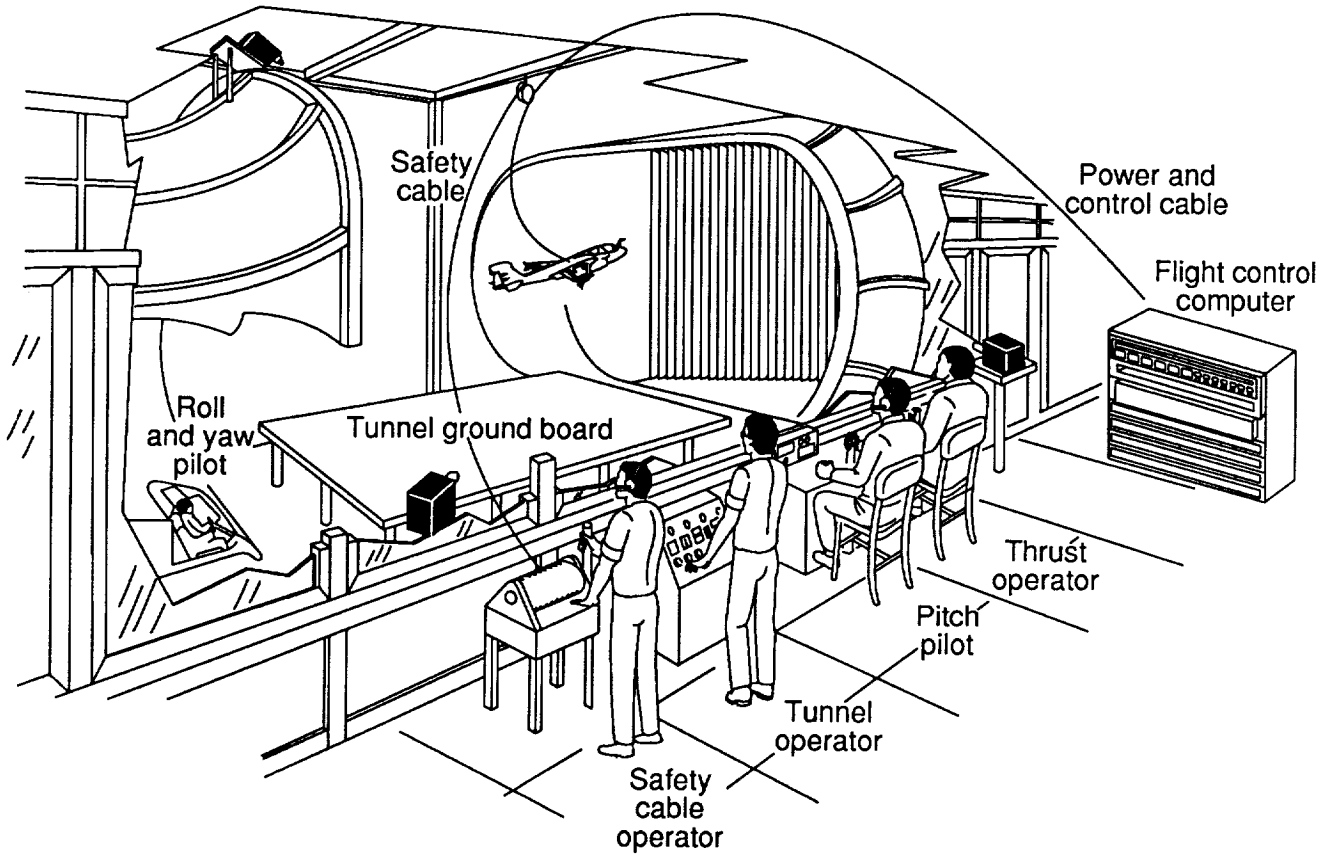

Figure 10. Test setup for free-flight test in Langley 30- by 60-Foot Tunnel.

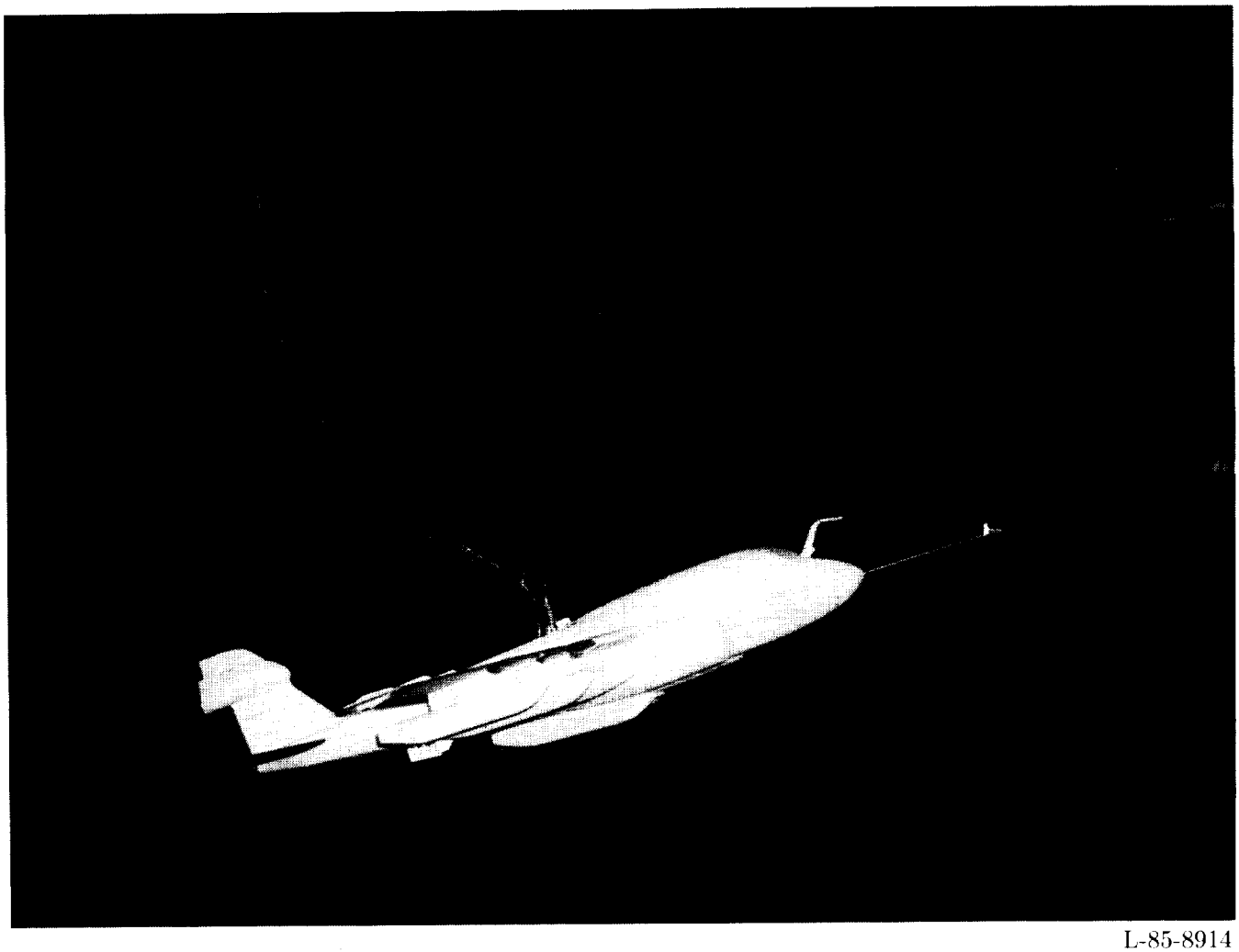

L-85-8914

Figure 11. Modified model in free-flight test.

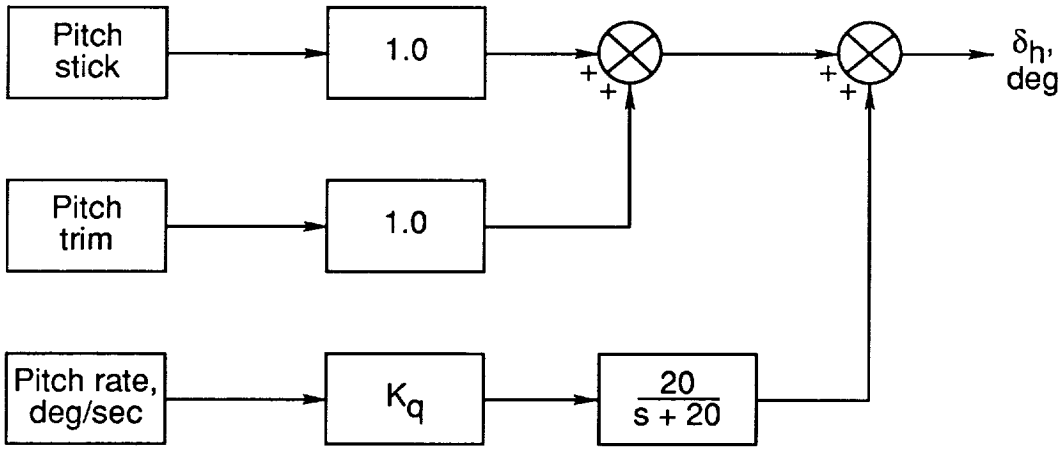

(a) Pitch.

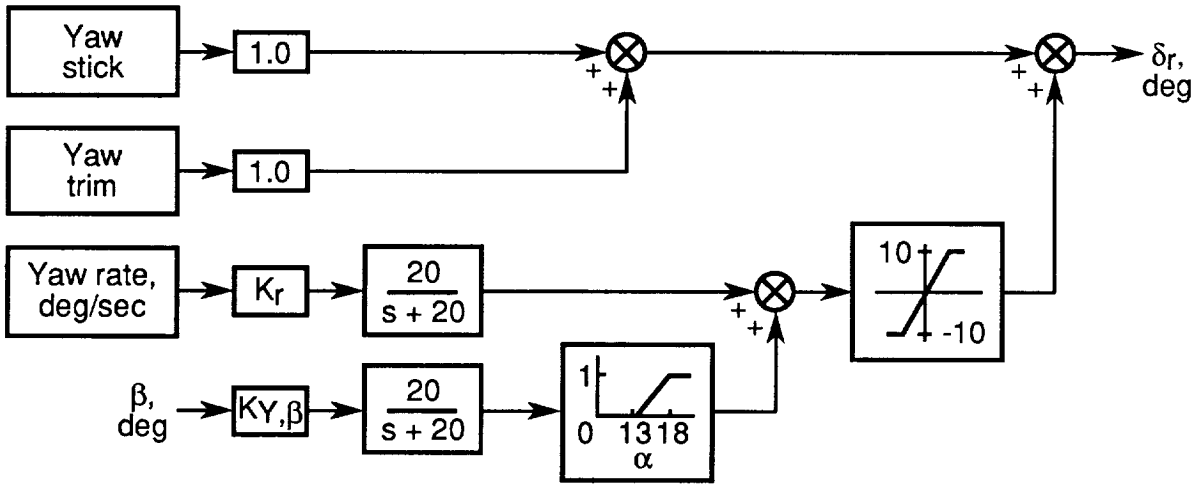

(b) Yaw.

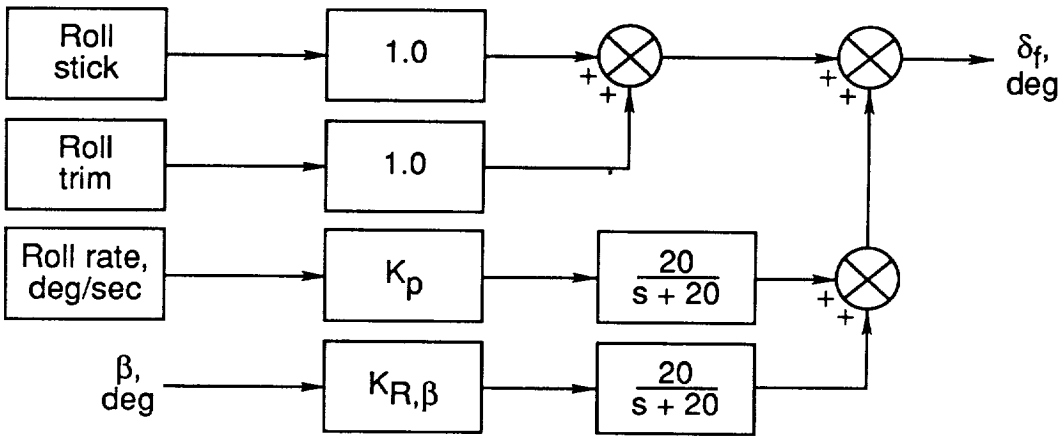

(c) Roll.

Figure 12. Control laws used in free-flight tests.

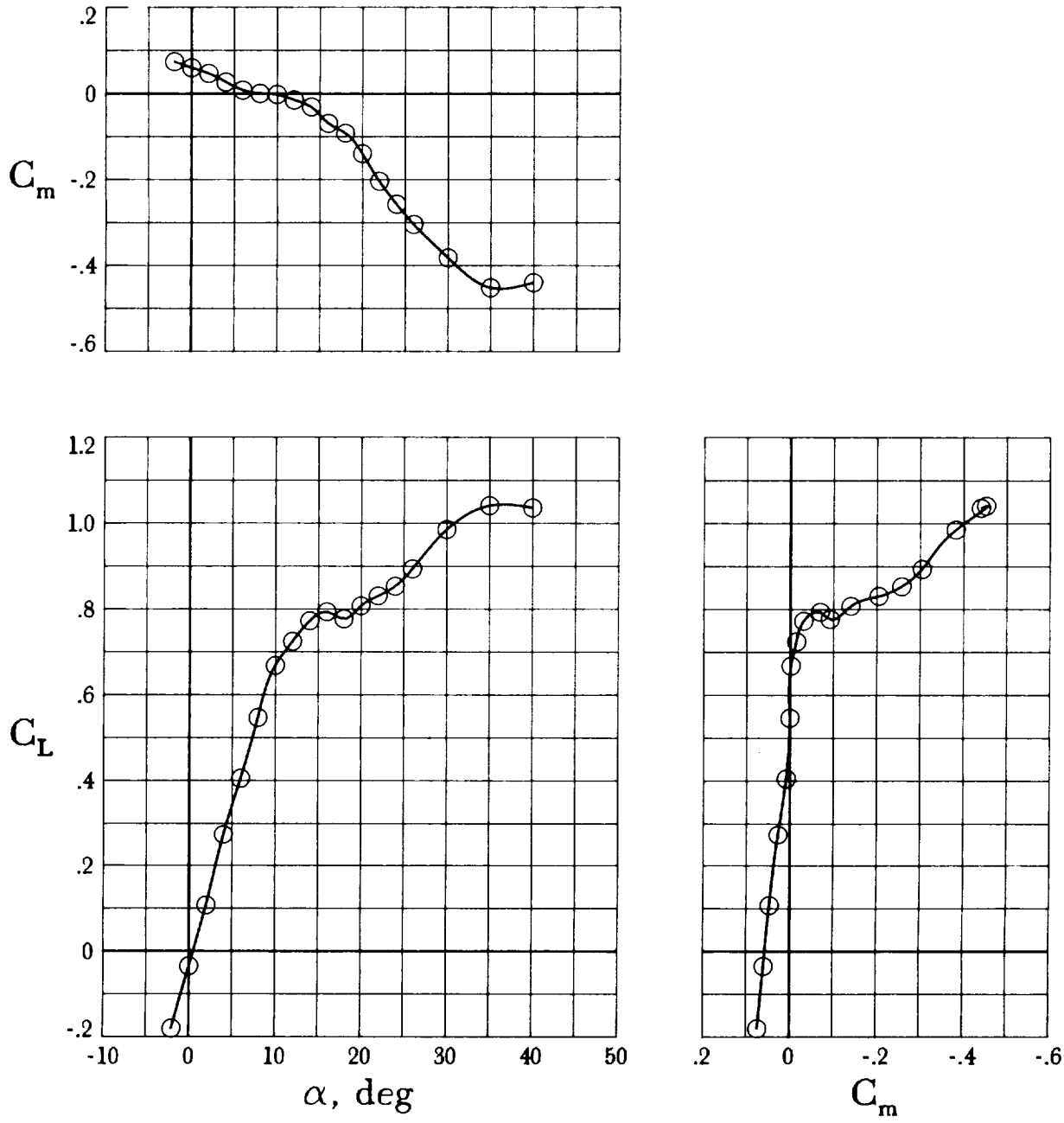

Figure 13. Static longitudinal aerodynamic characteristics of unmodified cruise configuration.

$\alpha = 4°$

$\alpha = 8°$

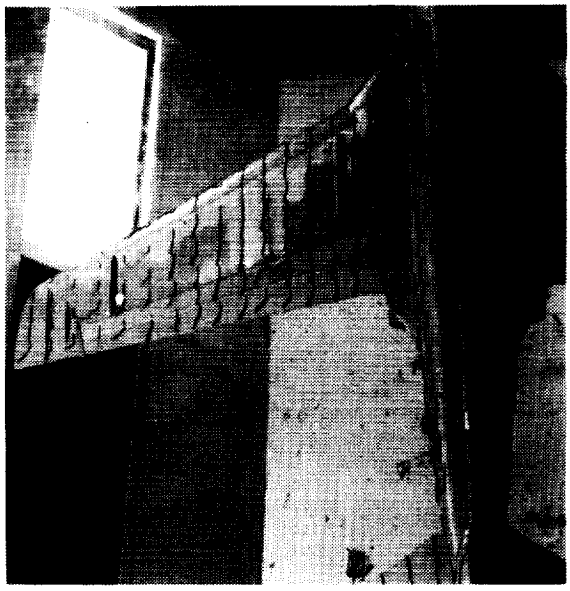

$\alpha = 10°$

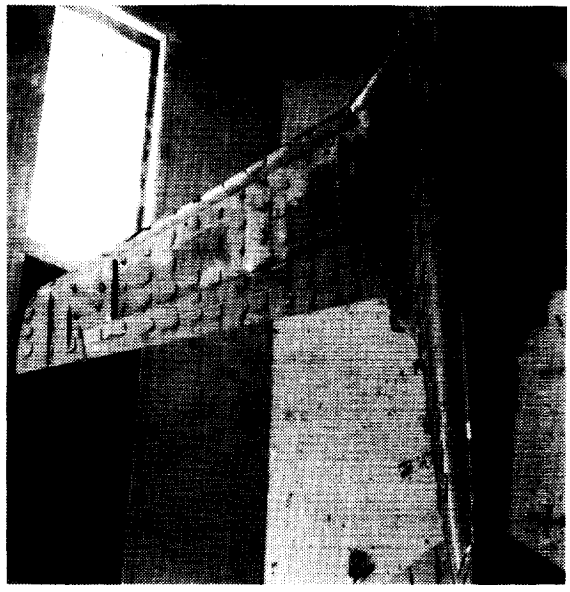

$\alpha = 12°$

L-92-04

Figure 14. Results of tuft studies at various angles of attack for cruise configuration with stores off.

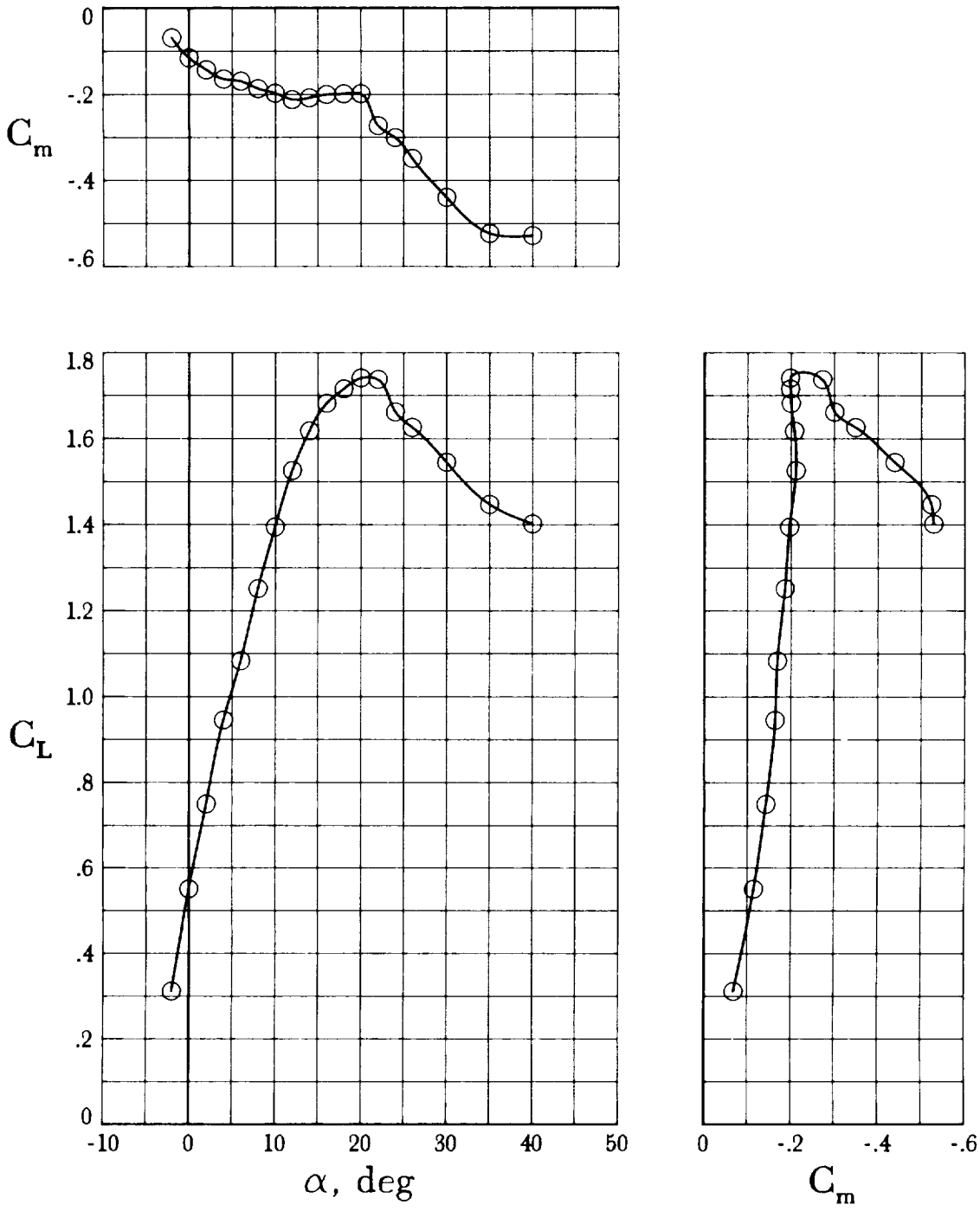

Figure 15. Static longitudinal characteristics of unmodified takeoff powered approach configuration. Slat/flap deflection, 27°/30°.

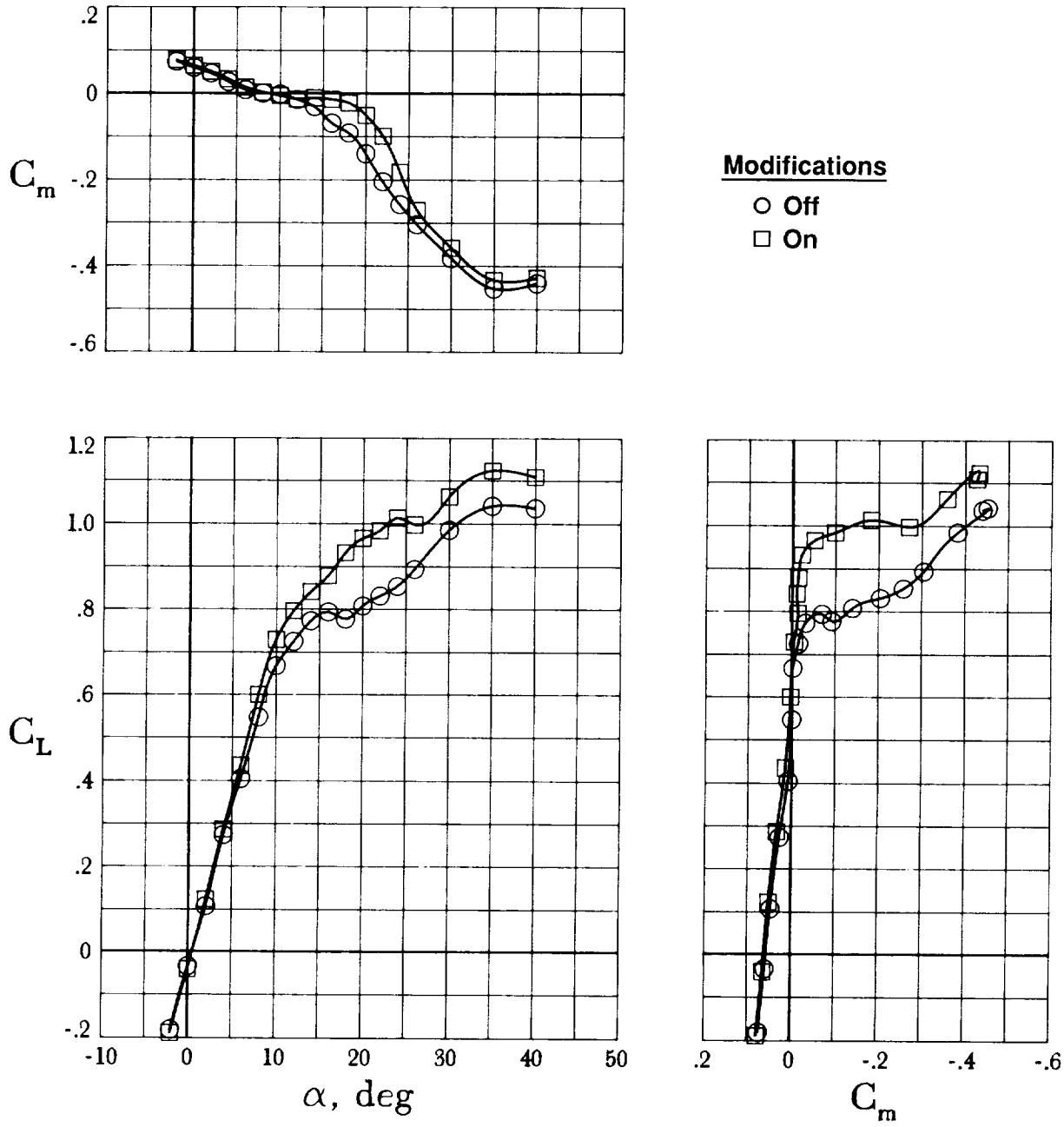

(a) Cruise configuration.

Figure 16. Effect of combined modifications on static longitudinal aerodynamic characteristics. Modifications include leading-edge glove strake, inboard leading-edge droop, vertical-tail extension, and modified wing-leading- and trailing-edge sections.

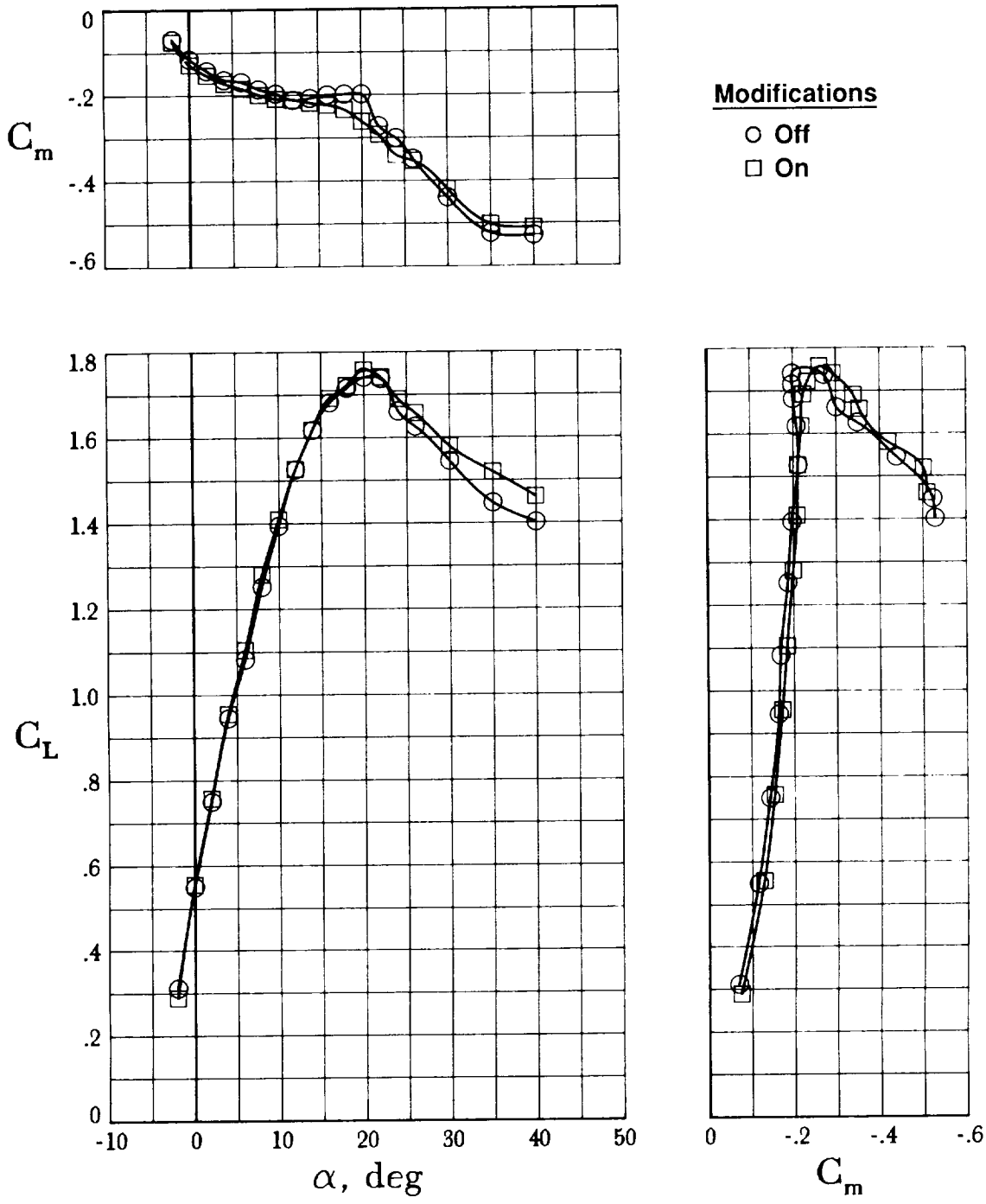

(b) Takeoff–powered approach configuration; slat/flap deflection, 27°/30°.

Figure 16. Concluded.

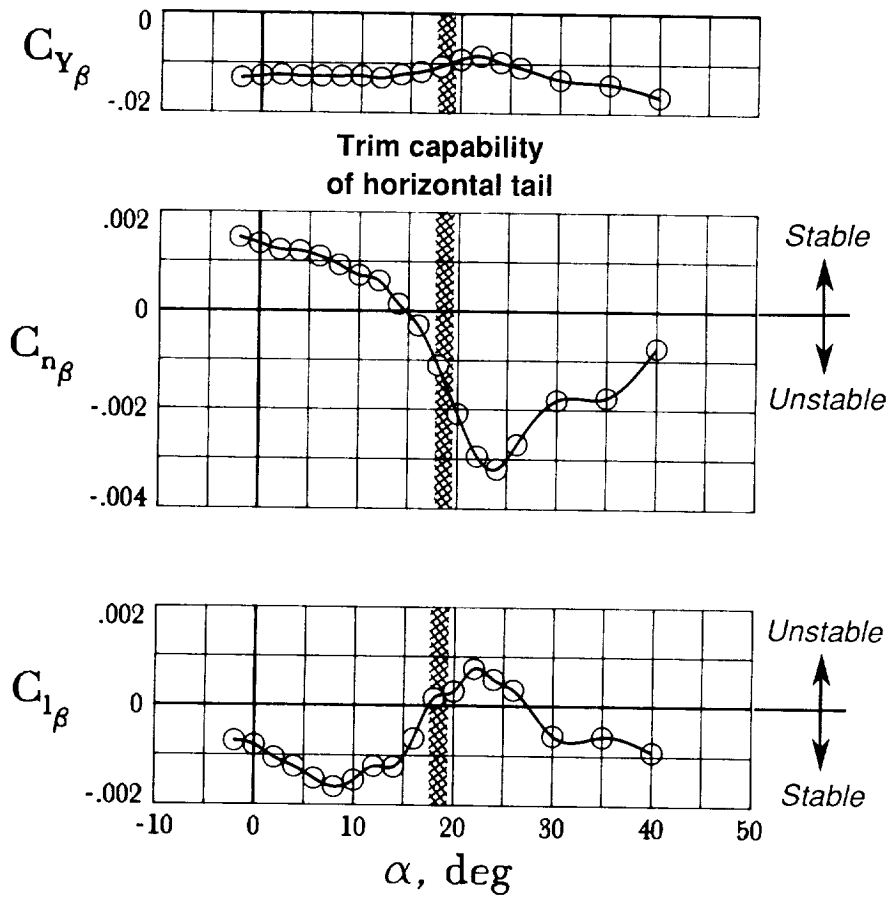

(a) Cruise configuration.

Figure 17. Variation of static lateral-directional stability derivatives with angle of attack.

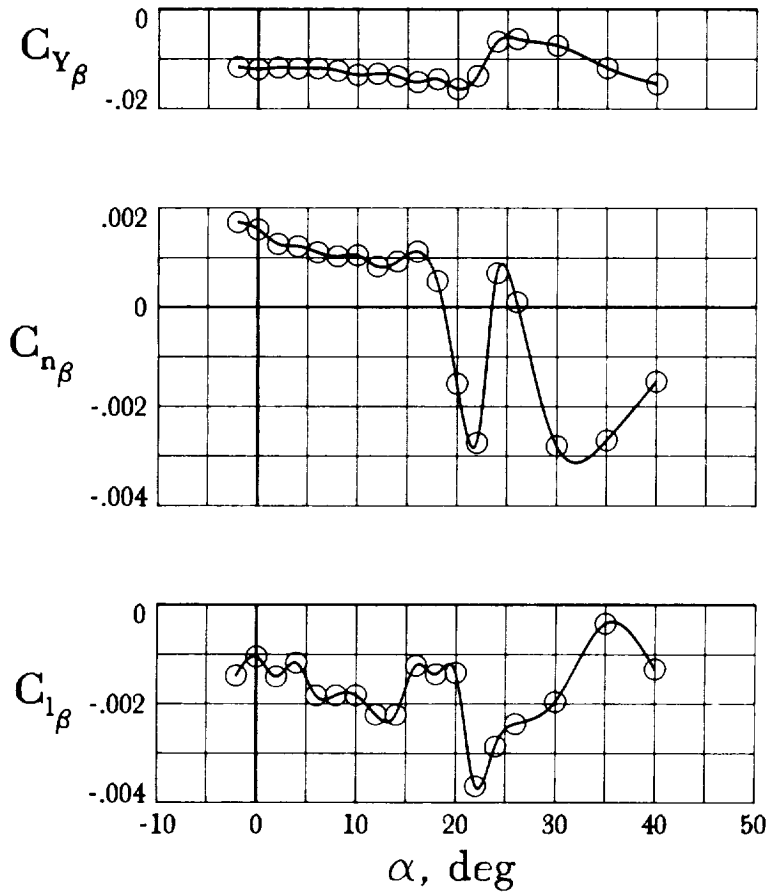

(b) Takeoff powered approach configuration; slat/flap deflection, 27°/30°.

Figure 17. Concluded.

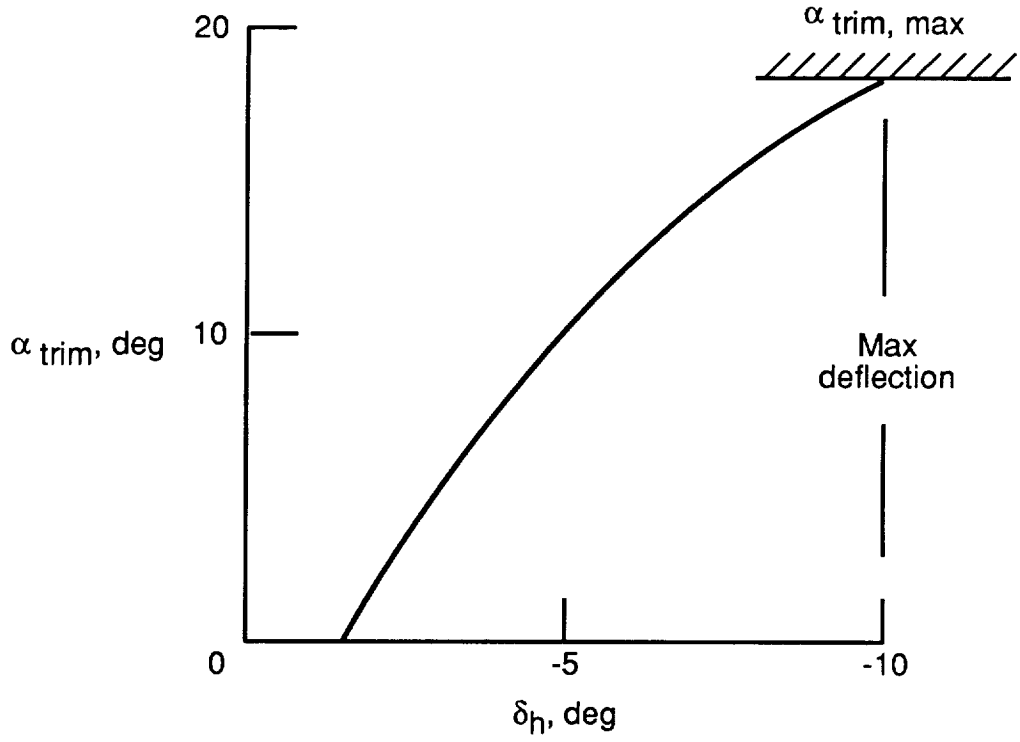

Figure 18. Angle-of-attack trim capability of horizontal tail.

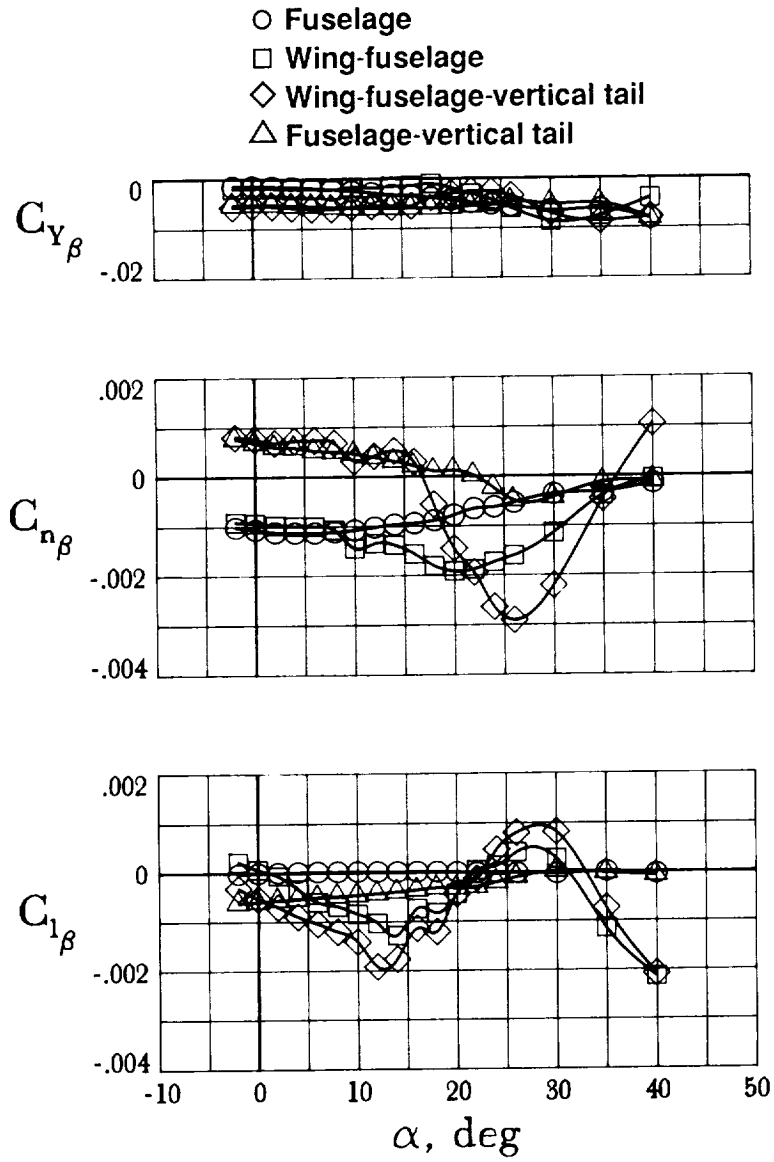

Figure 19. Effect of airframe components on static lateral-directional stability of cruise configuration with stores off.

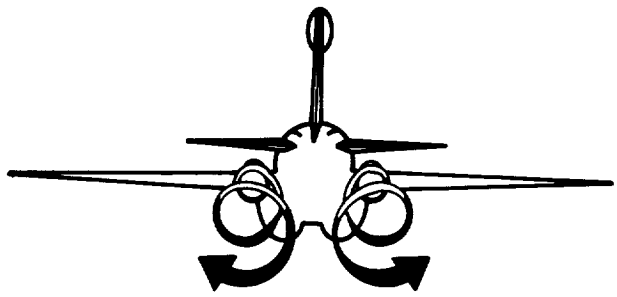

(a) Low angles of attack.

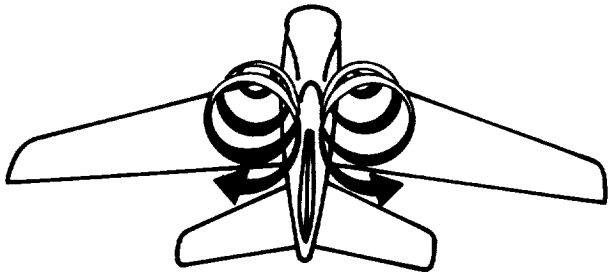

(b) Stall angles of attack.

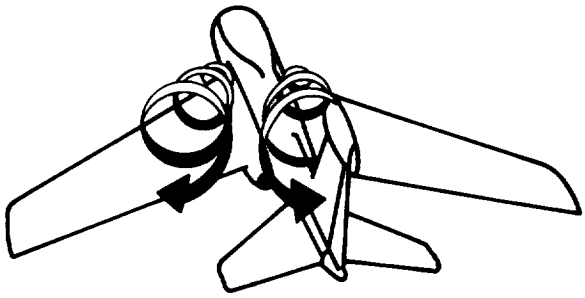

(c) Poststall angles of attack with sideslip.

Figure 20. Vortex system causing adverse (destabilizing) sidewash condition in sideslip.

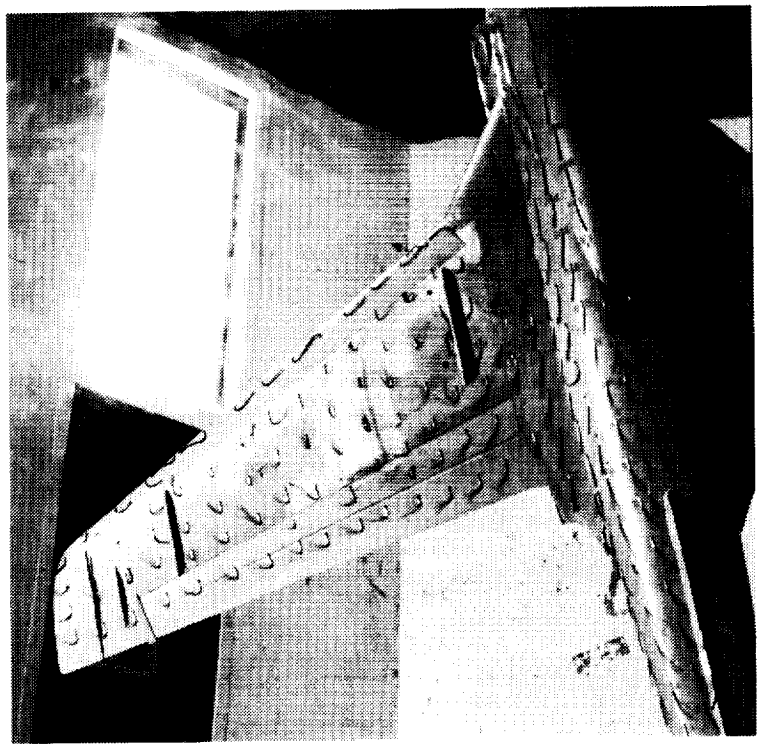

$\beta = 10°$

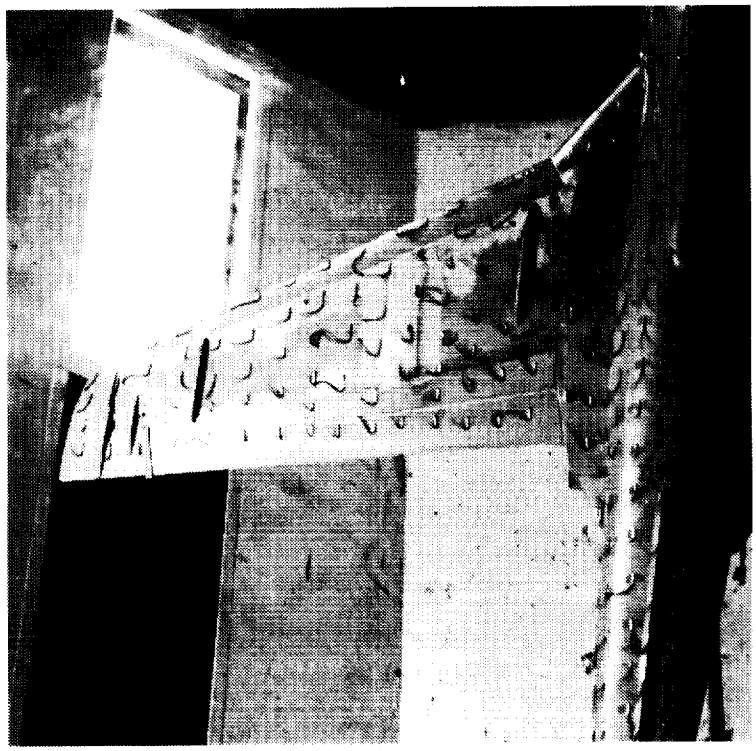

$\beta = -10°$

L-92-05

Figure 21. Results of tuft studies at $\alpha = 20°$ for cruise configuration with stores off.

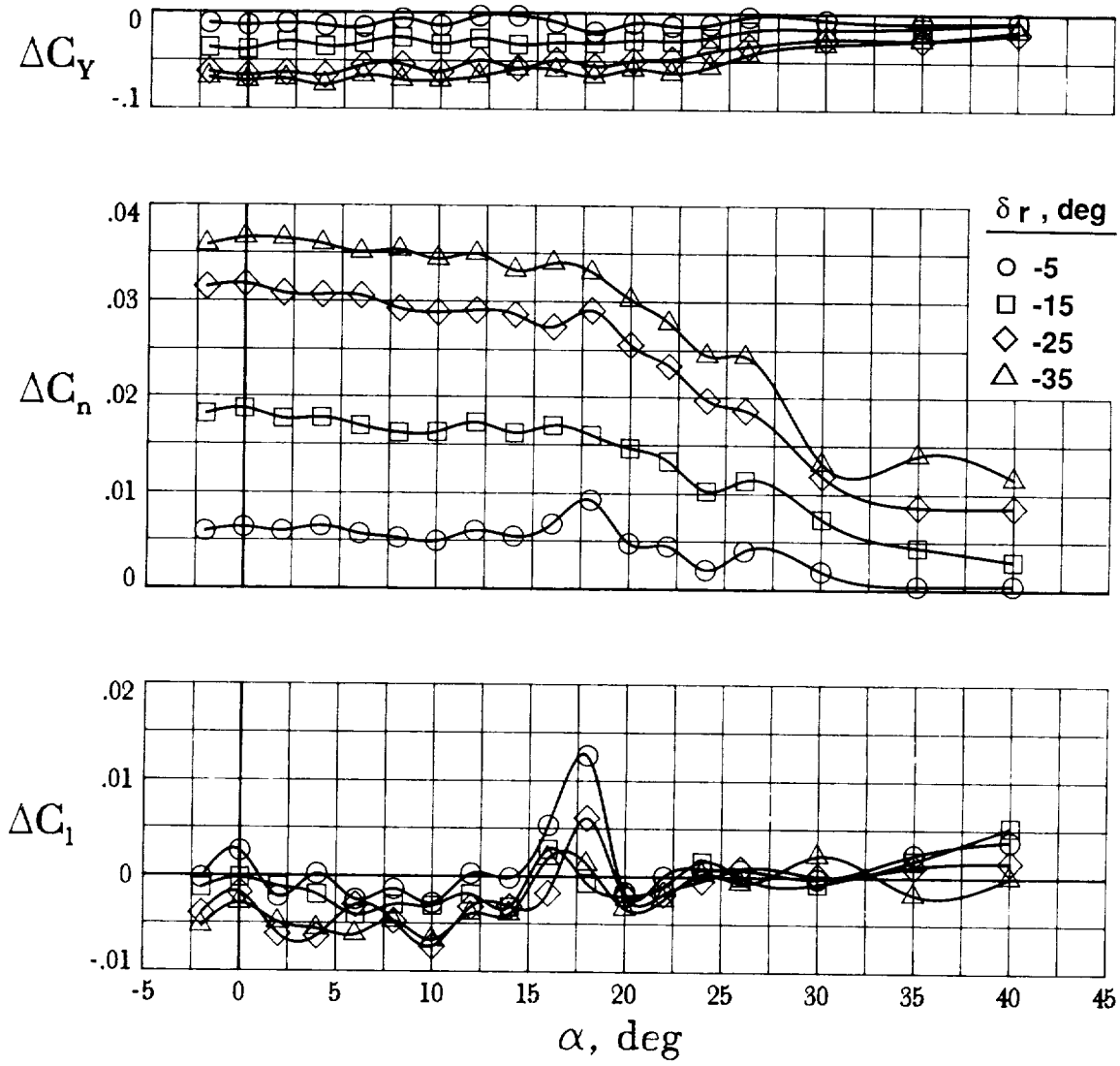

Figure 22. Effect of rudder deflection on cruise configuration. All other controls at 0°. $\beta = 0°$. Data from Langley 30- by 60-Foot Tunnel.

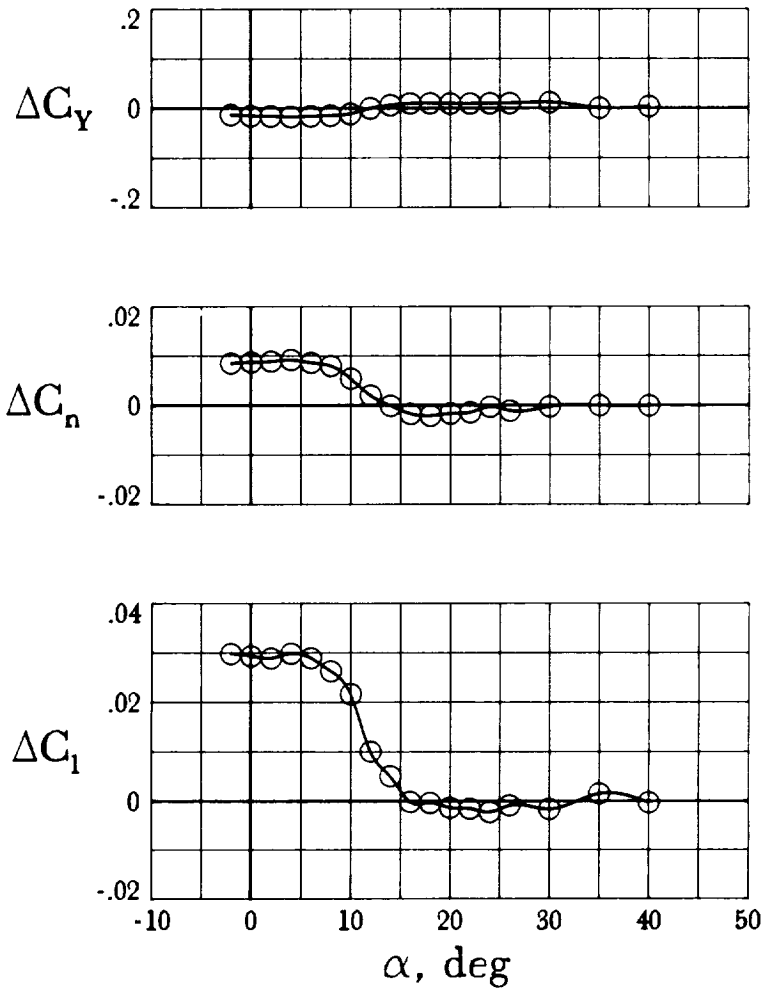

Figure 23. Effect of flaperon deflection on cruise configuration. All other controls at 0°. $\delta_f = 51°$; $\beta = 0°$.

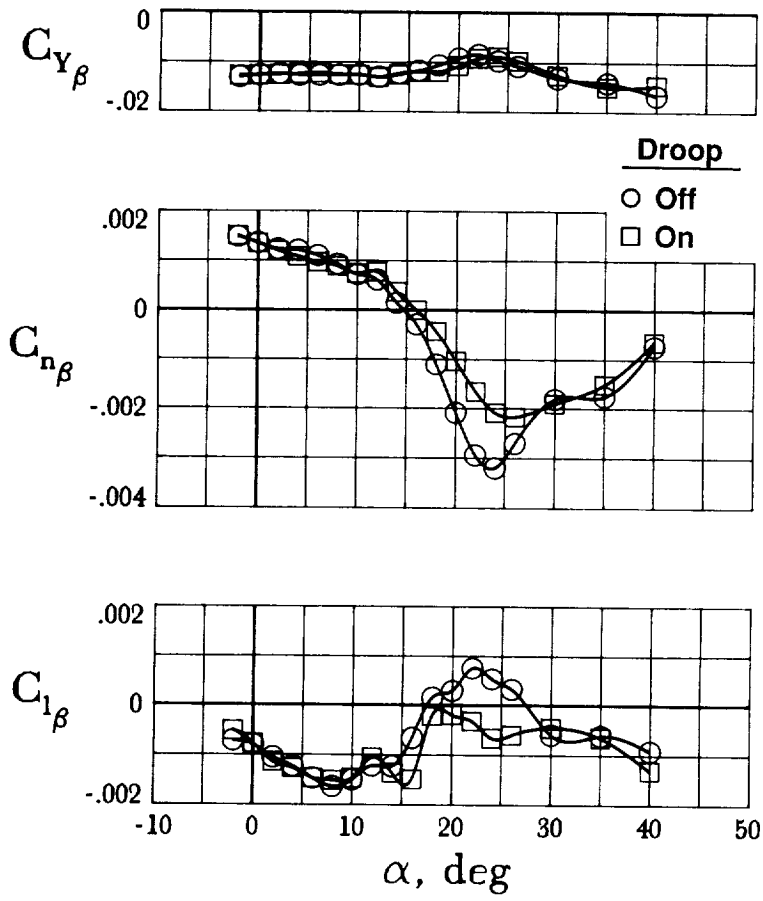

Figure 24. Effect of inboard wing-leading-edge droop on static lateral-directional stability of cruise configuration.

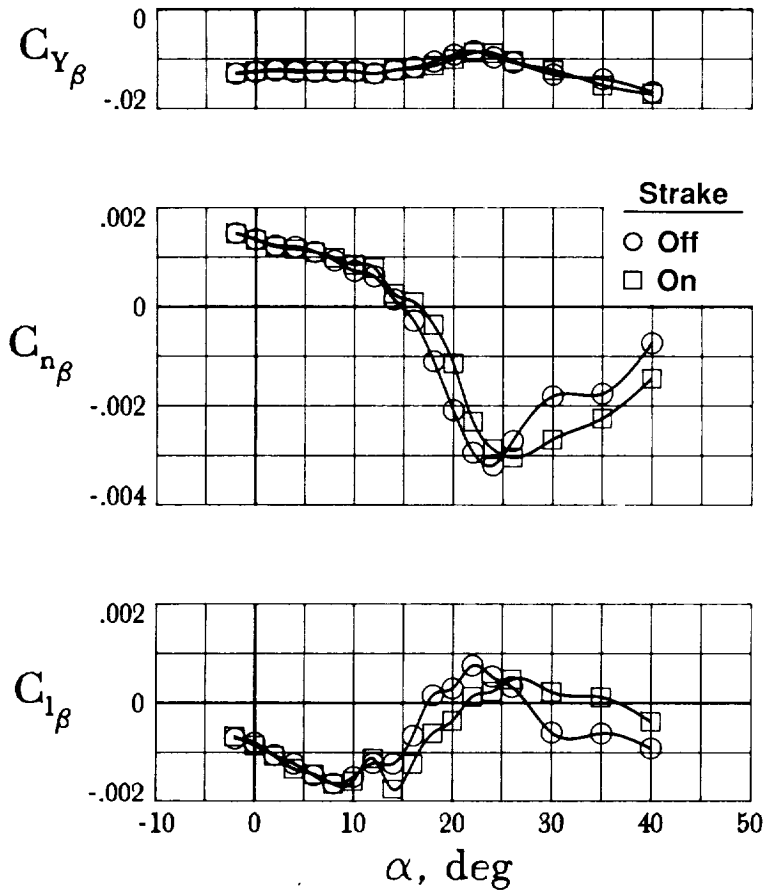

Figure 25. Effect of leading-edge glove strake on static lateral-directional stability of cruise configuration.

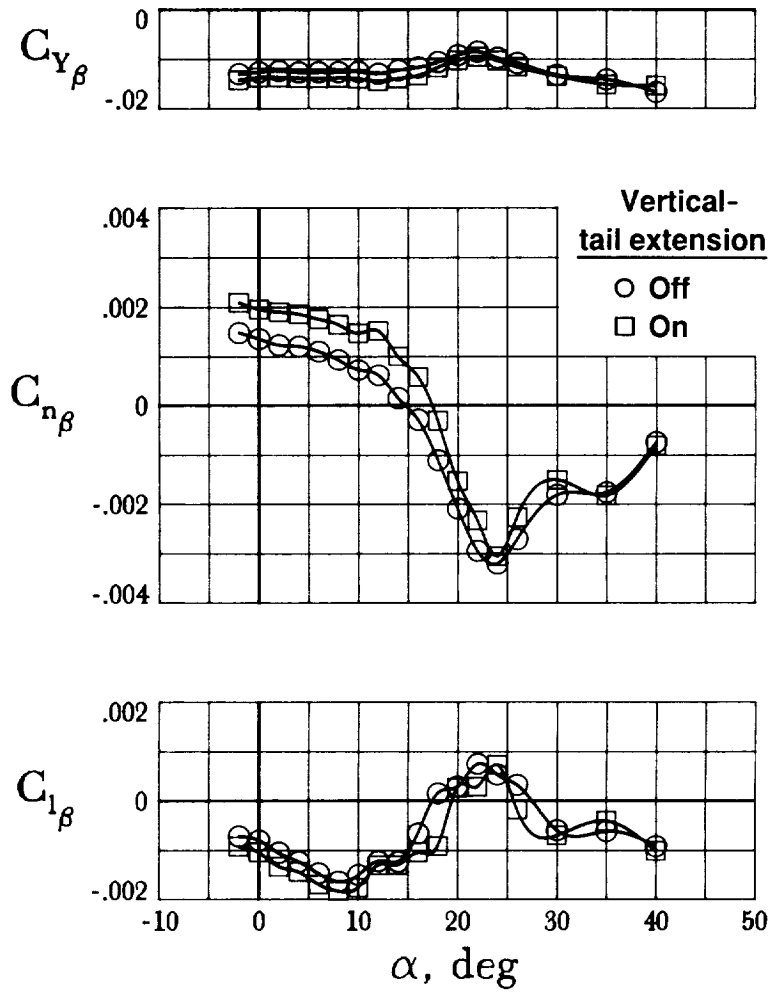

Figure 26. Effect of vertical-tail extension on static lateral-directional stability of cruise configuration.

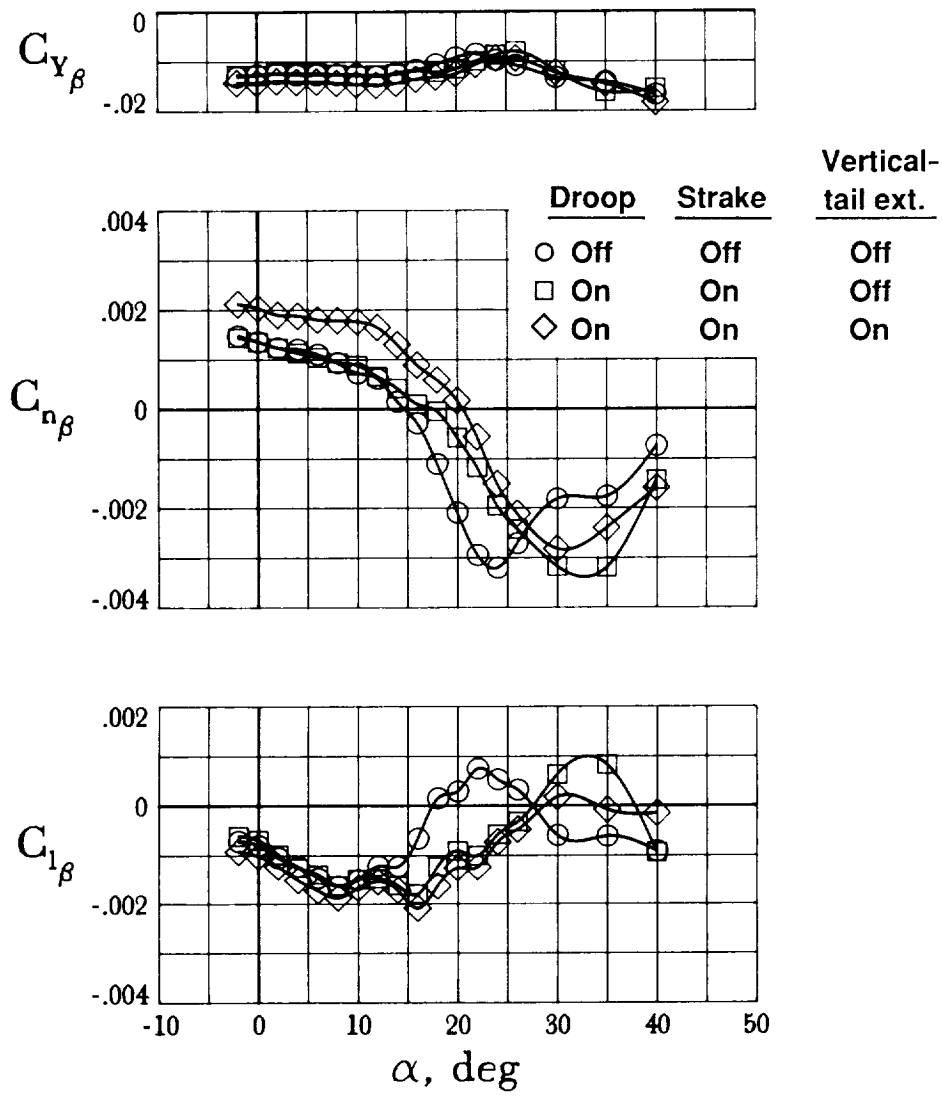

Figure 27. Combined effects of inboard wing-leading-edge droop, leading-edge glove strake, and vertical-tail extension on static lateral-directional stability of cruise configuration.

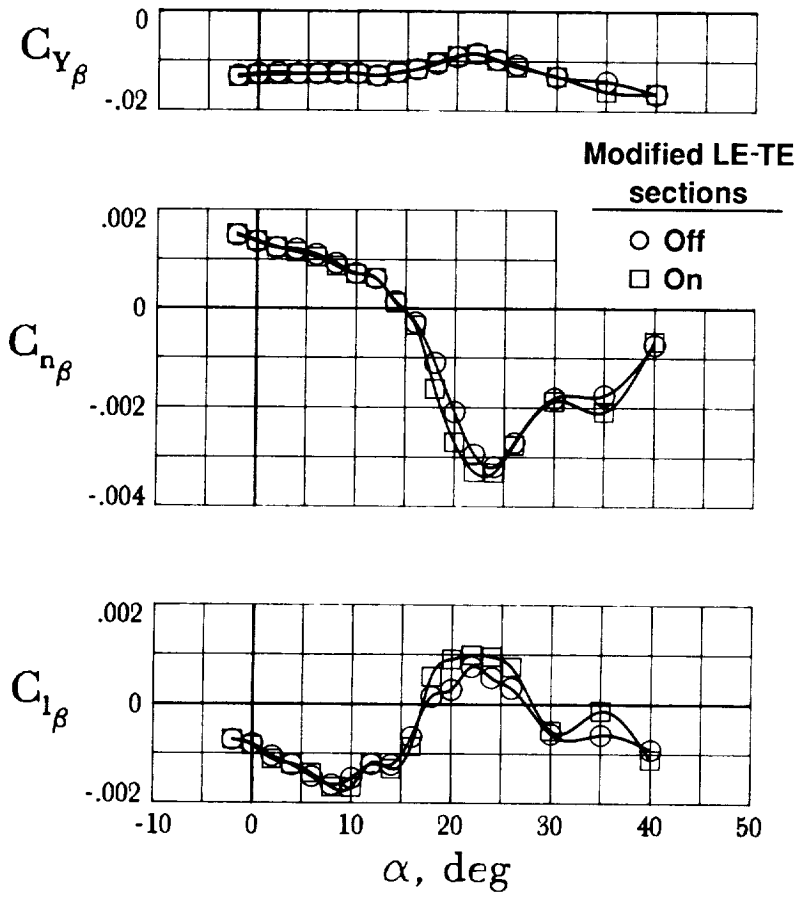

Figure 28. Effects of modified wing-leading-edge and trailing-edge sections on static lateral-directional stability of basic cruise configuration.

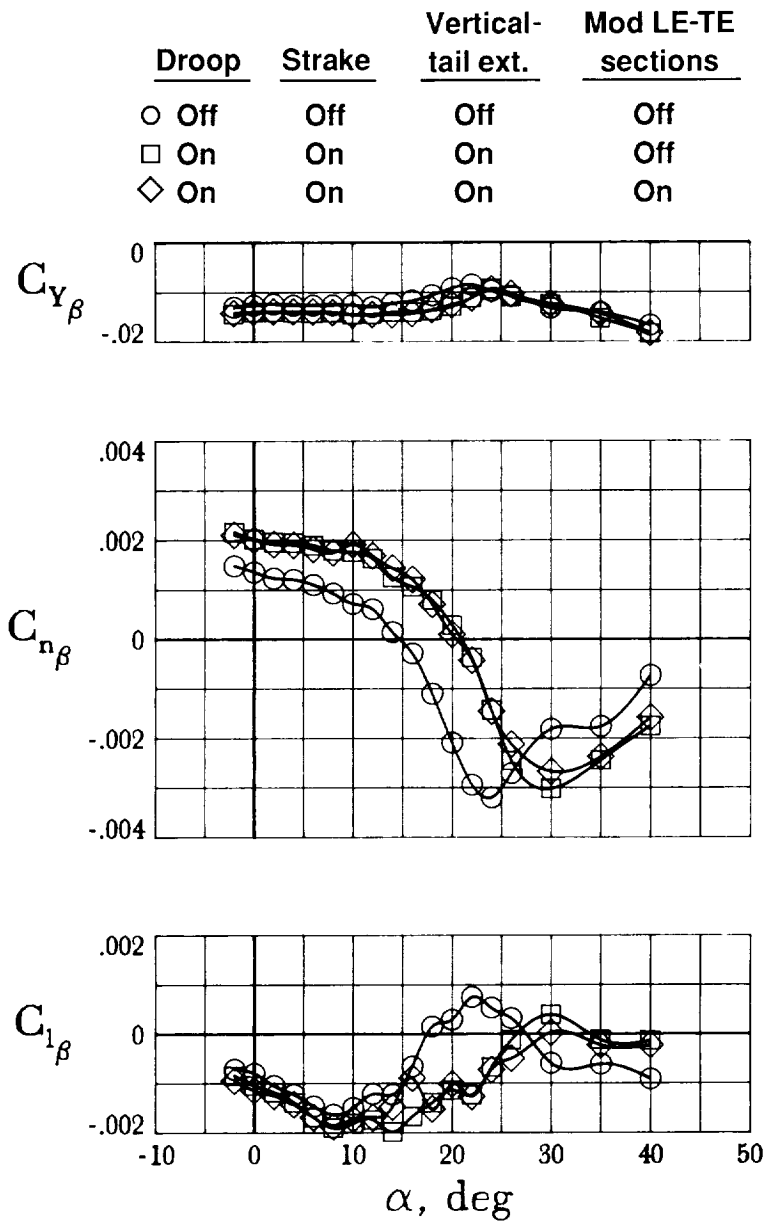

Figure 29. Effects of modified wing-leading-edge and trailing-edge sections on static lateral-directional stability of cruise configuration modified with wing-leading-edge droop, glove strake, and vertical-tail extension.

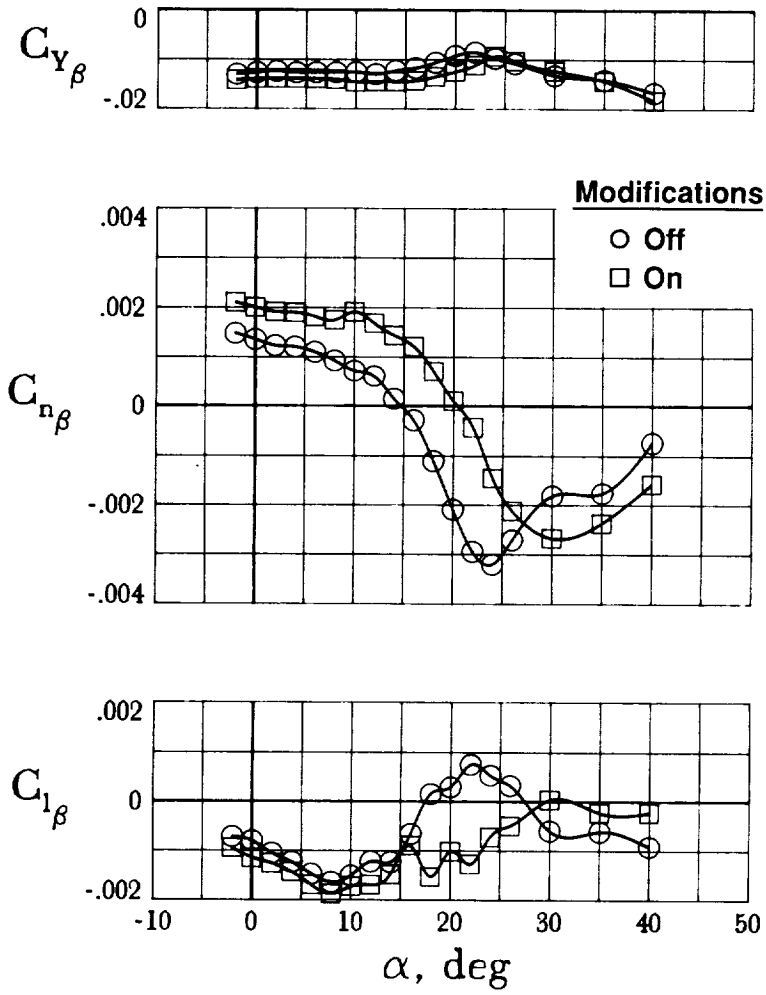

(a) Cruise configuration.

Figure 30. Effects of modifications on static lateral-directional stability characteristics. Modifications include leading-edge glove strake, inboard wing-leading-edge droop, vertical-tail extension, and modified wing leading edge and trailing edge.

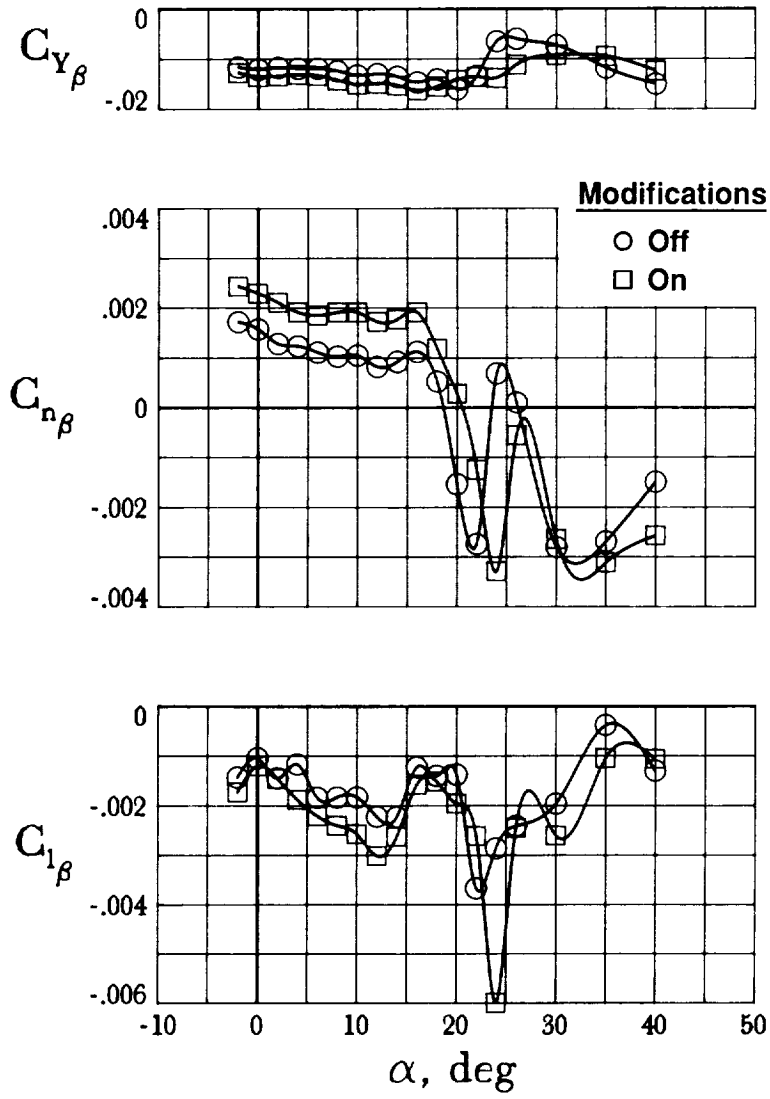

(b) Takeoff powered approach configuration; slat/flap deflection, 27°/30°.

Figure 30. Concluded.

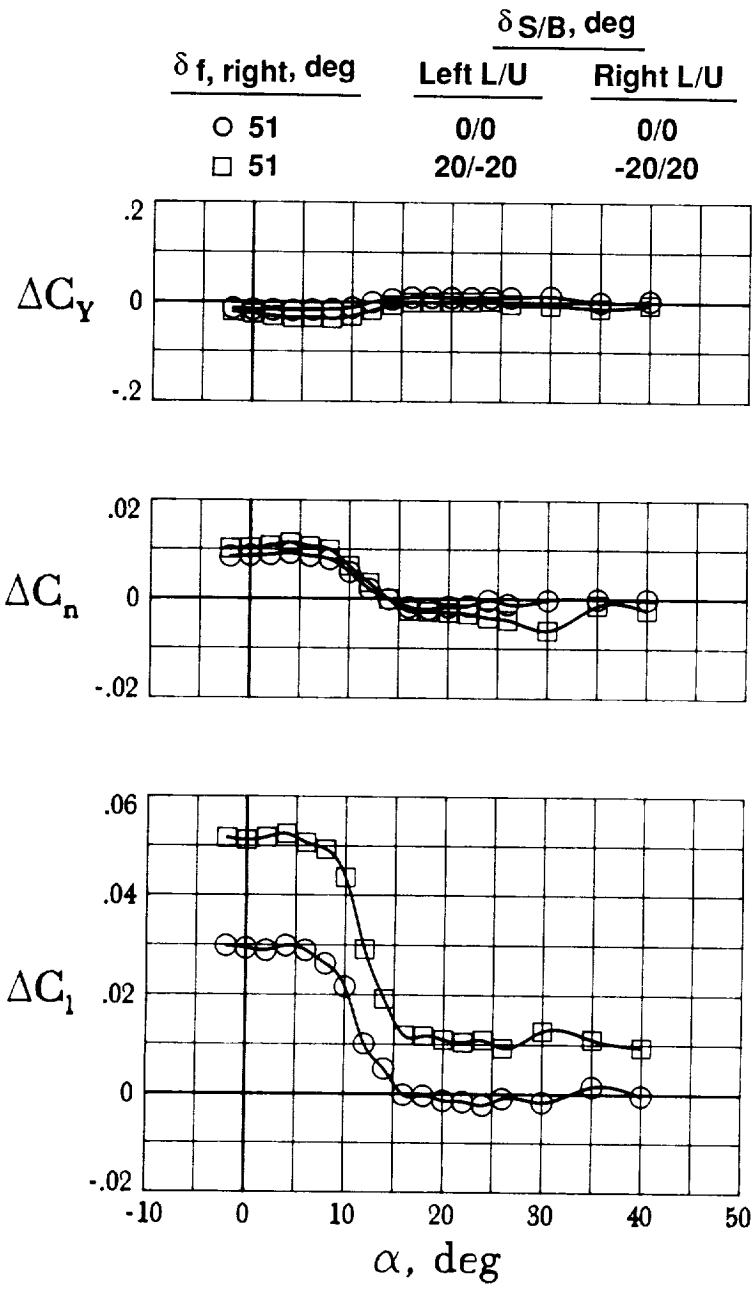

Figure 31. Effects of deflection of combined speed brake and flaperon on modified cruise configuration. All other controls at 0°. $\beta = 0°$.

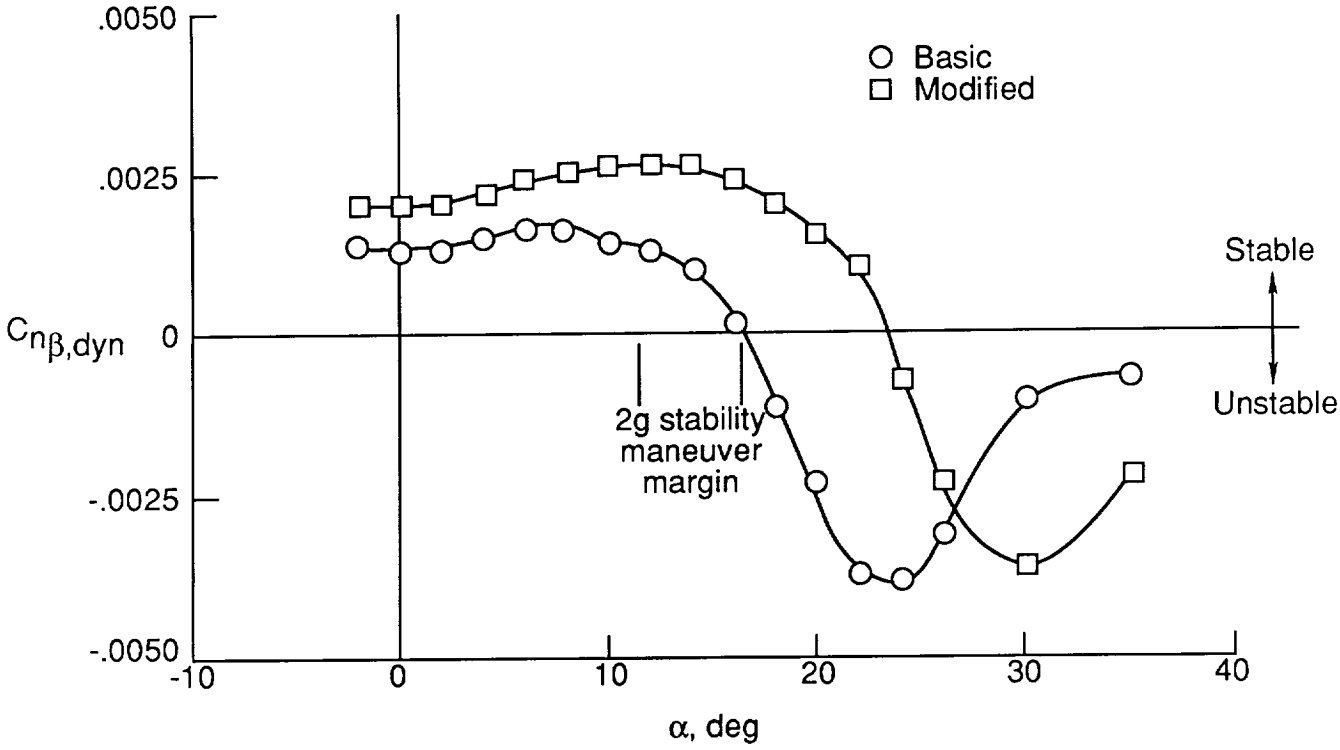

(a) Cruise configuration.

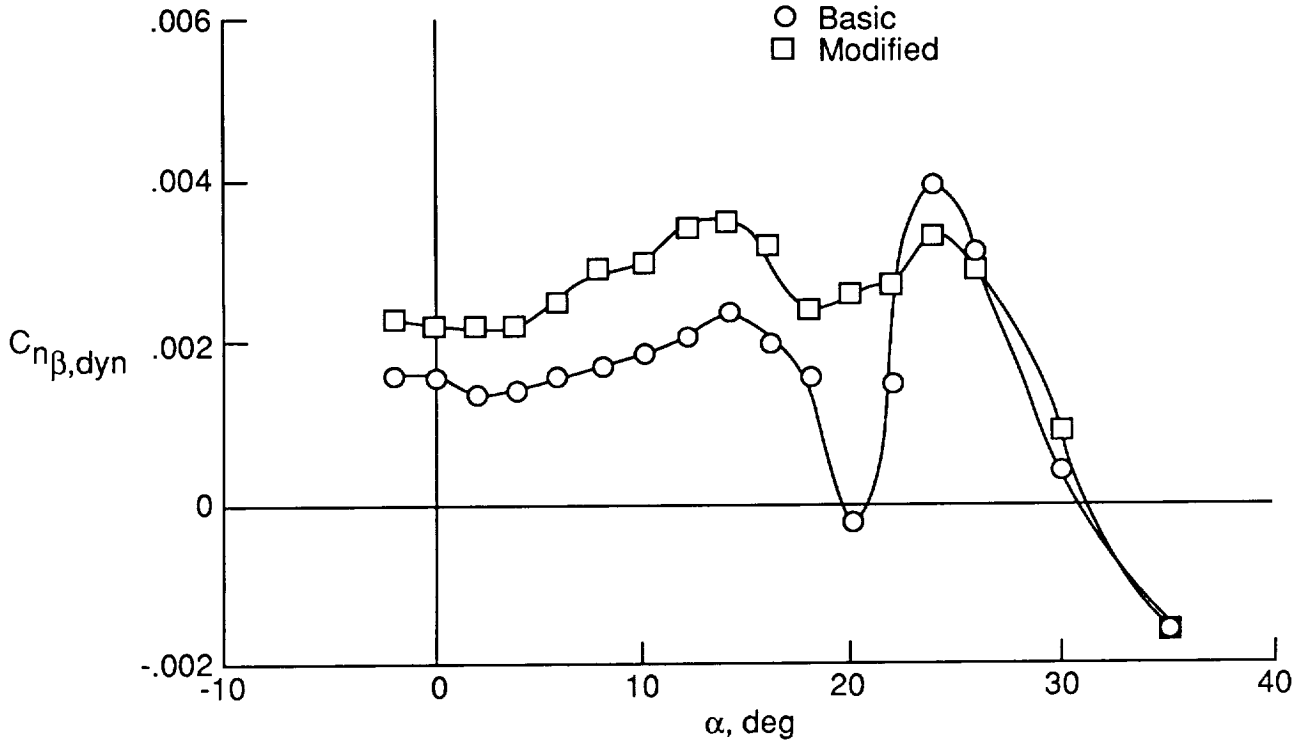

(b) Takeoff powered approach configuration; slat/flap deflection, 27°/30°.

Figure 32. Effect of modifications on departure resistance. Indicated stability margin is for 2g maneuver (60° bank angle), airspeed of 250 knots, and weight of 47 500 lb.

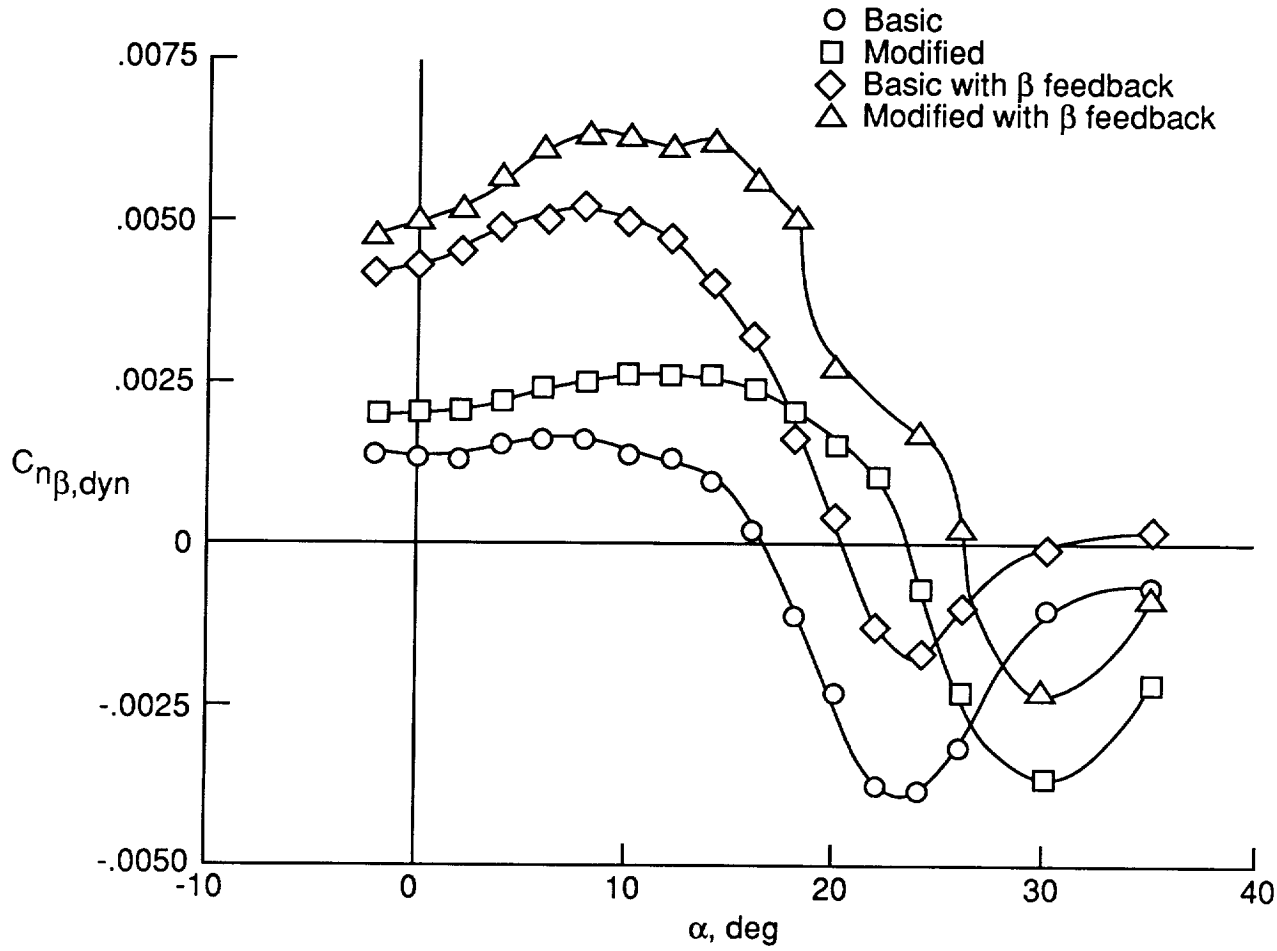

Figure 33. Effect of airframe and control-system modifications on departure resistance of cruise configuration. Normal controls modified with β feedback to rudder and flaperons.

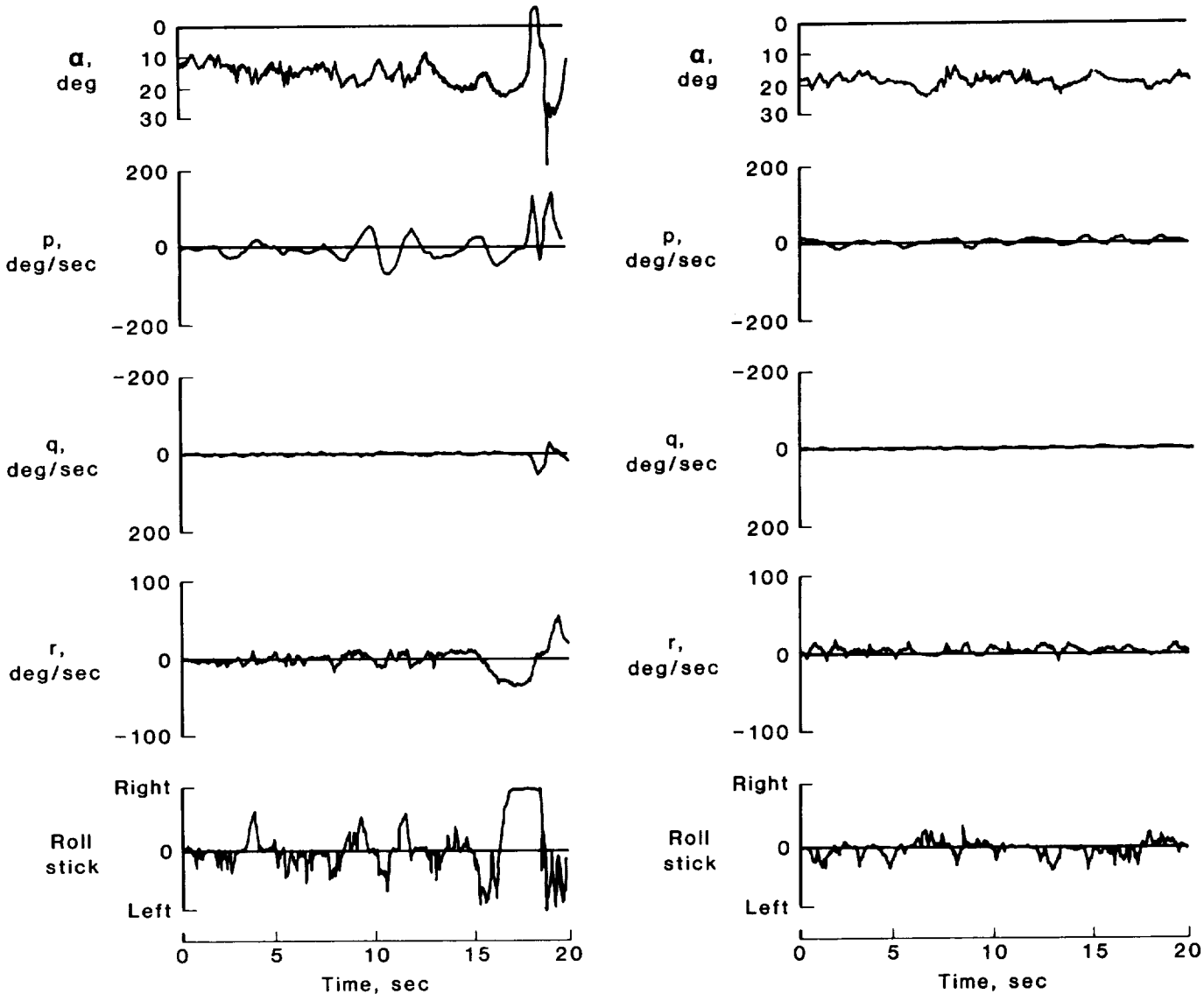

(a) Modifications off.

(b) Modifications on.

Figure 34. Effect of modifications on model flight characteristics. Modifications include leading-edge glove strake, inboard wing-leading-edge droop, vertical-tail extension, and modified wing-leading-edge and trailing-edge sections. Values shown are in model scale. High-angle-of-attack control system active.

REPORT DOCUMENTATION PAGE

Form Approved
OMB No. 0704-0188

1. AGENCY USE ONLY *(Leave blank)*	2. REPORT DATE	3. REPORT TYPE AND DATES COVERED
	May 1992	

4. TITLE AND SUBTITLE
Wind-Tunnel Static and Free-Flight Investigation of High-Angle-of-Attack Stability and Control Characteristics of a Model of the EA-6B Airplane

5. FUNDING NUMBERS
WU 505-61-71-07

6. AUTHOR(S)
Frank L. Jordan, Jr., and David E. Hahne

7. PERFORMING ORGANIZATION NAME(S) AND ADDRESS(ES)
NASA Langley Research Center
Hampton, VA 23665-5225

8. PERFORMING ORGANIZATION REPORT NUMBER
L-16813

9. SPONSORING/MONITORING AGENCY NAME(S) AND ADDRESS(ES)
National Aeronautics and Space Administration
Washington, DC 20546-0001

10. SPONSORING/MONITORING AGENCY REPORT NUMBER
NASA TP-3194

11. SUPPLEMENTARY NOTES

12a. DISTRIBUTION/AVAILABILITY STATEMENT
Unclassified Unlimited

Subject Category 02

12b. DISTRIBUTION CODE

13. ABSTRACT *(Maximum 200 words)*

An investigation was conducted in the Langley 30- by 60-Foot Tunnel and the Langley 12-Foot Low-Speed Tunnel to identify factors contributing to a directional divergence at high angles of attack for the EA-6B airplane. The study consisted of static wind-tunnel tests, smoke and tuft flow-visualization tests, and free-flight tests of a 1/8.5-scale model of the airplane. The results of the investigation indicate that the directional divergence of the airplane is brought about by a loss of directional stability and effective dihedral at high angles of attack. Several modifications were tested that significantly alleviate the stability problem. The results of the free-flight study show that the modified configuration exhibits good dynamic stability characteristics and could be flown at angles of attack significantly higher than those of the unmodified configuration.

14. SUBJECT TERMS	15. NUMBER OF PAGES
Stability and control; Dynamic stability; High angle of attack; Free flight	58
	16. PRICE CODE A04

17. SECURITY CLASSIFICATION OF REPORT	18. SECURITY CLASSIFICATION OF THIS PAGE	19. SECURITY CLASSIFICATION OF ABSTRACT	20. LIMITATION OF ABSTRACT
Unclassified	Unclassified		